

Spectroscopic and Decade-long Photometric Observations of the Contact Binary V2790 Ori: Evidence for a Brown Dwarf Companion and a Solar-like Magnetic Activity Cycle

SI-RUI WANG,¹ KAI LI,¹ QI-QI XIA,¹ DONG-YANG GAO,¹ XIANG GAO,¹ JING-YI WANG,¹ YA-NI GUO,¹ XING GAO,² AND GUO-YOU SUN³

¹*Shandong Key Laboratory of Space Environment and Exploration Technology, Institute of Space Sciences, School of Space Science and Technology, Shandong University, Shandong, China.*

²*Xinjiang Astronomical Observatory, 150 Science 1-Street, Urumqi 830011, China*

³*Xingming Observatory, Urumqi, Xinjiang, China*

ABSTRACT

We present 22 sets of light curves and one radial velocity curve for the W UMa-type total eclipse contact binary system V2790 Ori, derived by combining all available public photometric data, the photometric data in previous studies, and our own spectroscopic and decade-long photometric observations. Our simultaneous analysis of the light curves and radial velocity curve shows that V2790 Ori is a W-subtype contact binary with a mass ratio of $q = 0.322(\pm 0.001)$ and a shallow contact degree of $14.8(\pm 0.6)\%$. The orbital period analysis based on 445 eclipsing minima reveals a secular decrease at a rate of $\dot{P} = -3.18(\pm 0.75) \times 10^{-8} \text{ d yr}^{-1}$, superimposed with a cyclic variation with an amplitude of $A = 8.98(\pm 2.19) \times 10^{-4} \text{ d}$ and a period of $P_3 = 7.44(\pm 0.52) \text{ yr}$. The secular decrease is caused by AML via magnetic braking, while the cyclic period variation is explained by the light-travel time effect due to a third body, which is likely to be a brown dwarf. Furthermore, our analysis indicates a mass transfer from the more massive component to the less massive one at a rate of $1.22(\pm 0.29) \times 10^{-8} \text{ M}_\odot \text{ yr}^{-1}$. A model with a cool spot on each component was adopted to fit the O'Connell effect observed in the light curves. Since the O'Connell effect varies over time, we identified a solar-like magnetic activity cycle with a period of approximately 5.4 yr by analyzing the magnitude difference (Δm) at the two light maxima and the O'Connell effect ratio. In addition, evolutionary analysis suggests that V2790 Ori is a newly formed contact binary that evolved from a detached phase into the present contact configuration.

Keywords: Eclipsing binary stars (444) — Close binary stars (254) — W Ursae Majoris variable stars (1783) — Fundamental parameters of stars (555) — Stellar activity (1580) — Stellar evolution (1599)

1. INTRODUCTION

Contact binaries are a class of close binary systems in which both components fill their Roche lobes (Z. Kopal 1959). W Ursae Majoris (W UMa)-type eclipsing binaries are a subset of contact binaries, characterized by both components sharing a common convective envelope (CCE; L. B. Lucy 1968a,b). Due to their contact configuration and tidal deformation, these systems exhibit continuous out-of-eclipse luminosity variations in their light curves. The presence of CCE enables efficient mass and energy exchange between the components, resulting in nearly equal surface temperatures despite different masses (L. B. Lucy 1968a,b; G. P. Kuiper 1941). This leads to the primary and secondary eclipse depths of the light curve being nearly equal or differing insignificantly (S. B. Qian et al. 2014). The light variations caused by eclipses impose strong constraints on the orbital and geometric properties of the system, making W UMa-type contact binaries ideal laboratories for determining the fundamental physical parameters of their components. This is crucial for investigating the physical characteristics of binary systems and testing theories of binary evolution (S. Qian 2003; K. Yakut & P. P. Eggleton 2005; L. Li et al. 2007; Z. Eker et al. 2008; P. P. Eggleton 2012). W UMa-type contact binary systems are usually classified into two subtypes: A-subtype and W-subtype binaries (L. Binnendijk 1970). Compared to A-subtype contact binaries, W-subtype contact binaries generally have shorter orbital periods (R. C. Smith 1984), later spectral types, and their less massive component tends to have a higher surface temperature.

The orbital periods of W UMa-type contact binary systems are generally shorter than 0.7 day (R. W. Hilditch 2001), and are not constant over time. The secular variation of orbital period is primarily governed by mass transfer and angular momentum loss (AML) via magnetic braking (B. Paczynski 1971; F. van Veer 1979; T. Rahunen 1981; C. A. Tout & P. P. Eggleton 1988). Specifically, conservative mass transfer from the less massive to the more massive component results in an increase in the orbital period. In contrast, mass transfer in the reverse direction, AML, or a combination of AML and mass transfer can lead to a decrease in the period (e.g., K. Li et al. 2020; A. Poro et al. 2024, 2025). In addition to secular trends, many W UMa-type systems exhibit cyclic variations in their orbital period, as observed in V0599 Aur (K. Hu et al. 2020), OO Leo (Z.-B. Meng et al. 2024), and LX Lyn and V0853 Aur (X. Zhang & B. Zhang 2024). Such variations are often attributed to either magnetic activity cycle (J. H. Applegate 1992) or the light-travel time effect (LTTE) caused by a third body (e.g., J. B. Irwin 1952, 1959; P. Mayer 1990). According to these theories, the Applegate mechanism proposes that magnetic activity cycle in one or both components leads to variations in the gravitational quadrupole moment, thereby modulating the orbital period. While the LTTE produces apparent period changes in orbital period as the eclipsing binary orbits the barycenter of a triple system.

For most W UMa-type contact binary systems, the light curves exhibit asymmetries, which is known as the O'Connell effect (D. J. K. O'Connell 1951). The O'Connell effect has been attributed to several mechanisms, such as starspots due to stellar magnetic activity (L. Binnendijk 1960), hot spots caused by a mass-transferring gas stream or material accretion between the components (J. S. Shaw 1994), circumstellar material surrounding the binary (Q.-Y. Liu & Y.-L. Yang 2003), and asymmetric circumfluence caused by Coriolis forces (D.-Q. Zhou & K.-C. Leung 1990). Among these, starspots are the most commonly used explanation for the O'Connell effect (N. J. Wilsey & M. M. Beaky 2009; K. Li et al. 2014; M. F. Knote et al. 2022). Owing to their later spectral types, W-subtype contact binaries typically show more intense magnetic activity. In some contact binaries, the O'Connell effect remains nearly stable. However, similar to sunspots that follow an 11-year cycle, certain systems exhibit solar-like magnetic activity cycles, which can naturally lead to a quasi-periodic variation in the O'Connell effect (e.g., N.-P. Liu et al. 2020; M. Yilmaz et al. 2023; J.-J. Wang et al. 2025). The long-term periodic variations in the orbital period, on timescales of several years to decades, may also serve as indirect evidence of such magnetic cycles. If W UMa-type contact binaries do possess magnetic activity cycles, long-term photometric observation is essential for their investigations.

V2790 Ori (TYC 1322-294-1, GSC 01322-00294) was first identified as a short-period W UMa-type contact binary system by S. A. Otero et al. (2004) based on the public data release of the Northern Sky Variability Survey (NSVS; P. R. Wozniak et al. 2004). Its orbital period was reported to be $P = 0.287842$ d with a primary minimum at HJD 2451521.695 (S. A. Otero et al. 2004). S. J. Gettel et al. (2006) estimated its distance to be 199 pc and reported that the V -band magnitude ranges from $V_{\max} = 11.181$ to $V_{\min} = 11.743$. V2790 Ori has been studied by E. J. Michaels (2016), W. Kriwattanawong & K. Kriwattanawong (2019), A. Shokry et al. (2020), and K. B. Alton & K. Stępień (2021) based only on photometric observations spanning approximately one year. The determined physical parameters and orbital period variation analyses in previous studies are summarized in Table A1. However, because the photometric data and the eclipsing minima used for analysis cover different time spans, and the O'Connell effect in the light curves changes over time, their derived results are not identical. For example, while the derived physical parameters remain nearly unchanged, the derived spot parameters are not consistent. W. Kriwattanawong & K. Kriwattanawong (2019) reported an increase in the orbital period, whereas K. B. Alton & K. Stępień (2021) found a period decrease superimposed with a cyclic variation. In addition, the significant and variable O'Connell effect in the light curves suggests the presence of a solar-like magnetic activity cycle. The discrepancies among previous studies, together with the possible presence of a solar-like magnetic activity cycle, demonstrate the need for further detailed investigation of V2790 Ori. In this study, we combined all available photometric data with our own decade-long photometric and spectroscopic observations, constructing the most extensive data set for V2790 Ori to date. The simultaneous analysis of light and radial velocity curves enables us to derive reliable absolute physical parameters, providing a solid foundation for investigating the orbital period variation, magnetic activity cycle, and evolutionary status of V2790 Ori.

2. OBSERVATIONS AND DATA REDUCTION

2.1. Photometric Observations

From 2015 to 2025, long-term multiband photometric observations of V2790 Ori were carried out by three ground-based telescopes located in China. The telescopes are: (1) the Weihai Observatory 1.0 m Cassegrain telescope of Shandong University (WHOT; S. M. Hu et al. 2014), equipped with a PIXIS 2048B CCD, providing a field of view of $12' \times 12'$; (2) the 60 cm Ningbo Bureau of Education and Xinjiang Observatory Telescope (NEXT), equipped with an FLI PL23042 CCD, producing a field of view of $22' \times 22'$; (3) the 85 cm telescope at the Xinglong Station of the National Astronomical Observatories (XL85), equipped with an Andor DZ936 CCD, offering a field of view of $32' \times 32'$. These telescopes are all equipped with Standard Johnson-Cousin-Bessel BVR_CI_C filters. The detailed photometric observation log is listed in Table 1.

All CCD images were reduced using the PHOT package of IRAF¹. After performing bias and flat corrections, a comparison star and a check star were selected in the same CCD field of view near V2790 Ori. The comparison star is 2MASS J06154200+1938278 ($V_{\text{mag}} = 10.928$, $B - V = 0.724$, $J - K = 0.481$), and the check star is 2MASS J06151951+1937076 ($V_{\text{mag}} = 11.159$, $B - V = 0.144$, $J - K = 0.185$). The differential magnitudes between the target and the comparison star, as well as between the comparison and check stars, were obtained using aperture photometry and differential photometry methods. Table A2 lists the Barycentric Julian Date (BJD) and the differential magnitudes (Δm) of the reduced observational data.

To more accurately investigate the variations of the O'Connell effect, we examined other available light curves. Photometric data from the American Association of Variable Star Observers (AAVSO)² and the Transiting Exoplanet Survey Satellite (TESS; G. R. Ricker et al. 2015) were analyzed in this study as well. We downloaded and organized all available data from the AAVSO International Database. The details of the light curves used for the subsequent analysis are listed in Table 1. Although E. J. Michaels (2016) have analyzed the photometric data from AAVSO, their study only covers data from 2015. We also reanalyzed photometric data from the study of W. Kriwattanawong & K. Kriwattanawong (2019) and A. Shokry et al. (2020).

TESS observes approximately 150 million stars brighter than 16 magnitude in the TESS band, with a photometric precision ranging from 60 ppm to 3%, enabling a wide array of stellar astrophysics investigations (R. J. Oelkers & K. G. Stassun 2018). The photometric data are publicly available via the Mikulski Archive for Space Telescopes (MAST)³. We searched the TESS data for V2790 Ori and found that it was observed in Sector 43, Sector 44, and Sector 45 at a 10-minute cadence, and in Sector 71 and Sector 72 at a 200-second cadence. Each sector was observed continuously for about 27.4 days, specifically spanning 2021 September 16 to October 11 (Sector 43), October 12 to November 5 (Sector 44), November 7 to December 2 (Sector 45), 2023 October 17 to November 11 (Sector 71), and 2023 November 12 to December 7 (Sector 72). Additionally, the raw data in Sector 43, Sector 44, Sector 45, and Sector 71 have been calibrated by the Science Processing and Operations Center (SPOC) pipeline (J. M. Jenkins et al. 2016), which provides Pre-search Data Conditioning Simple Aperture Photometry flux (PDCSAP). However, the TESS-SPOC data in Sector 43 and Sector 45 are of relatively poor quality, and no TESS-SPOC data are available for Sector 71. Therefore, we carried out photometry for these sectors. We downloaded 20×20 pixel TESS full-frame image (FFI) cutouts (C. E. Brasseur et al. 2019) from MAST using the lightkurve package (Lightkurve Collaboration et al. 2018). The aperture and background masks were then created to extract light curves by selecting an appropriate threshold, and the light curves were detrended using the Savitzky-Golay filter (T. E. Oliphant 2007). All the flux obtained were normalized and converted to magnitudes using the following equation: $mag = -2.5 \log(flux)$. To save computational time, the TESS data were binned to 1000 points by averaging.

All light curves are phase folded using the following linear ephemeris:

$$T = T_0 + 0.287842 \times E, \quad (1)$$

where T represents the observed time, T_0 is the primary minimum of each light curve, determined via the K-W method (K. K. Kwee & H. van Woerden 1956), based on photometric data from WHOT, XL85, NEXT, AAVSO, and TESS. The orbital period of 0.287842 d is adopted from S. A. Otero et al. (2004), and E is the cycle number. Finally, a total of 22 sets of phase-folded light curves are obtained. As shown in Figure 1, the primary minimum is distinctly flat-bottomed, indicating that V2790 Ori undergoes a total eclipse. The two maxima of each light curve are clearly unequal, and the difference between them varies over time. This phenomenon demonstrates that V2790 Ori exhibits a significant and time-variable O'Connell effect, which is worth further investigation.

2.2. Spectroscopic Observations

A total of 20 spectra of V2790 Ori were obtained using the Beijing Faint Object Spectrograph and Camera (BFOSC) mounted on the 2.16 m telescope at Xinglong Observatory (XL216; Z. Fan et al. 2016), including 8 spectra acquired on 2019 December 30 and 12 spectra on 2021 November 17. For BFOSC, the grating E9+G10 and a 1''.6-wide slit oriented in the south-north direction were employed. This setup provides a spectral resolution of $R \sim 11000$ per pixel, covering a wavelength range from 3300 Å to 10000 Å. We also obtained spectra of HD 65583 (K0, $V_{\text{mag}} = 7.00$), which serves as a radial velocity standard star. The exposure times of HD 65583 were set to 300 s for the 2019 observations and 200 s for the 2021 observations. Detailed information about the spectroscopic observations is listed in Table 1.

The BFOSC spectroscopic data were reduced by the NOAO package in IRAF, including bias subtraction, flat correction, cosmic-ray removal, one-dimensional spectrum extraction, and wavelength calibration. Following these procedures, the normal-

¹ IRAF is distributed by the National Optical Astronomy Observatory (NOAO), which is operated by the Association of the Universities for Research in Astronomy, Inc., under cooperative agreement with the National Science Foundation (NSF; <http://iraf.noao.edu/>).

² <https://www.aavso.org/>

³ <https://mast.stsci.edu/portal/Mashup/Clients/Mast/Portal.html>

Table 1. Observation Log of V2790 Ori

| Photometric Observations | | | | |
|----------------------------|-------------------------------|--------------------------|--------------------|-------------------------|
| Date of Observation | Band (Exposure time (s)) | Mean errors (mag) | Type | Data Source |
| 2015 Feb 05 & Mar 06 | $B(30)/V(20)/R_C(15)/I_C(10)$ | 0.007/0.008/0.007/0.009 | Light curve | WHOT |
| 2015 Dec 07 | $B(30)/V(15)$ | 0.013/0.013 | Minimum | WHOT |
| 2015 Dec 28 | $B(30)/V(15)/R_C(10)/I_C(8)$ | 0.010/0.008/0.006/0.008 | Light curve | WHOT |
| 2016 Feb 20 | $V(8)$ | 0.008 | Minimum | WHOT |
| 2016 Mar 30 | $V(10)$ | 0.014 | Minimum | WHOT |
| 2016 Nov 05 | $V(10)$ | 0.006 | Minimum | WHOT |
| 2016 Dec 30 | $B(30)/V(15)/R_C(10)/I_C(8)$ | 0.010/0.020/0.007/0.007 | Light curve | WHOT |
| 2017 Mar 01 | $V(10)$ | 0.011 | Minimum | WHOT |
| 2017 Sep 11 | $V(10)$ | 0.022 | Minimum | WHOT |
| 2017 Dec 20 | $B(30)/V(15)/R_C(10)/I_C(8)$ | 0.012/0.007/0.006/0.007 | Light curve | WHOT |
| 2017 Oct 01 | $V(20)$ | 0.007 | Minimum | WHOT |
| 2018 Dec 27 | $B(30)/V(20)/R_C(15)/I_C(15)$ | 0.007/0.005/0.006/0.006 | Light curve | XL85 |
| 2019 Dec 29 & 2020 Jan 03 | $B(18)/V(10)/R_C(7)/I_C(10)$ | 0.009/0.009/0.009/0.008 | Light curve | NEXT |
| 2020 Dec 20 | $B(30)/V(15)/R_C(8)/I_C(5)$ | 0.018/0.013/0.011/0.013 | Light curve | WHOT |
| 2021 Jan 04 & Jan 05 | $B(18)/V(10)/R_C(7)/I_C(10)$ | 0.006/0.006/0.011/0.006 | Light curve | NEXT |
| 2022 Jan 02 | $B(30)/V(15)/R_C(10)/I_C(8)$ | 0.008/0.0011/0.008/0.010 | Light curve | WHOT |
| 2022 Dec 31 | $B(30)/V(12)/R_C(9)/I_C(8)$ | 0.004/0.0004/0.004/0.004 | Light curve | XL85 |
| 2024 Feb 27 & Mar 08 | $B(40)/V(20)/R_C(10)/I_C(8)$ | 0.006/0.006/0.007/0.004 | Light curve | WHOT |
| 2025 Jan 08 | $B(30)/V(12)/R_C(9)/I_C(8)$ | 0.007/0.0007/0.007/0.009 | Light curve | XL85 |
| 2015 Jan 08 – Jan 29 | $g'/r'/i'$ | — | Light curve | AAVSO (Edward Michaels) |
| 2015 Nov 19 & Nov 20 | B/V | — | Light curve | AAVSO (Edward Michaels) |
| 2016 Mar 12 | V | — | Minimum | AAVSO (Kenneth Menzies) |
| 2017 Jan 02 | V | — | Minimum | AAVSO (Kenneth Menzies) |
| 2020 Jan 29 – Feb 05 | $B/V/I_C$ | — | Light curve | AAVSO (Kevin Alton) |
| 2024 Sep 21 | V | — | Minimum | AAVSO (Sjoerd Dufoer) |
| 2015 Jan 21 – Jan 23 | $B(120)/V(60)/R_C(60)$ | — | Light curve | TNO |
| 2017 Jan 21 & Jan 22 | $V/R_C/I_C$ | 0.008/0.0008/0.009 | Light curve | KAO |
| Spectroscopic Observations | | | | |
| Time (UT) | Number of Frames | Exposure (s) | Signal Noise Ratio | Telescope |
| 2019 Dec 30 | 8 | 900 | 33 – 43 | XL216 |
| 2021 Nov 17 | 12 | 900 | 67 – 92 | XL216 |

NOTE— Mean errors for each band represent the photometric accuracy of the system, which were estimated by calculating the standard deviation of the differential magnitudes between the comparison and check stars; TNO data are from [W. Kriwattanawong & K. Kriwattanawong \(2019\)](#); KAO data are from [A. Shokry et al. \(2020\)](#).

ized spectral data covering the wavelength range of 4706–5625 Å were obtained. We used the cross-correlation function (CCF) ([T. Szalai et al. 2007](#); [G. Matijević et al. 2010](#)) with HD 65583 to measure the radial velocities. The peak positions of the CCF curves were determined using the GaussPy+ package ([M. Riener et al. 2019](#)). A single peak is visible near phases 0 and 0.5, while double peaks appear at other phases. The derived radial velocities are listed in Table A3. Phases were computed using Equation (1), adopting $T_0 = \text{BJD } 2458847.25856$ for the 2019 observations and $T_0 = \text{BJD } 2459220.30069$ for the 2021 observations. The radial velocity curve was then analyzed using rvfit⁴ ([R. Iglesias-Marzoa et al. 2015](#)), an IDL-based code that fits radial

⁴ <http://www.cefca.es/people/~riglesias/rvfit.html>

velocity curves of binary systems through an adaptive simulated annealing global minimization algorithm. From the fitting, the mass ratio $q = 3.31(\pm 0.08)$ and systemic velocity $V_\gamma = -43.84(\pm 0.56) \text{ km s}^{-1}$ were initially derived for V2790 Ori.

3. RADIAL VELOCITY AND LIGHT CURVE ANALYSIS

In order to obtain the accurate physical parameters of V2790 Ori, we employed the 2015 version of the Wilson–Devinney (W-D) program (R. E. Wilson & E. J. Devinney 1971; R. E. Wilson 1979, 1990) to analyze the 22 sets of phase-folded light curves and radial velocity curve of V2790 Ori simultaneously. The initial value of the mass ratio was then set to $q = 3.31$, and the systemic velocity V_γ was initialized as -43.84 km s^{-1} .

It should be noted that both the rvfit and W-D programs adopt the mass ratio in the form of $q = M_2/M_1$ by default. Since the initial mass ratio is greater than 1, the less massive component is completely eclipsed by the more massive component during the total eclipse at phase 0. This enables a more precise determination of the effective temperature of the more massive component from the spectrum near phase 0. University of Lyon Spectroscopic analysis Software (ULySS; M. Koleva et al. 2009) was employed to determine the atmospheric parameters of the more massive component. ULySS performs the spectral fitting by matching the observed spectrum to a model one generated by an interpolator based on the ELODIE stellar library (P. Prugniel & C. Soubiran 2001). The atmospheric parameters are then derived by minimizing the residuals between the two spectra using a nonlinear least-squares algorithm. The observed spectrum obtained with BFOSC at phase 0.943 and the corresponding fitted spectra are shown in Figure A1 with black lines and red lines respectively. The obtained atmospheric parameters of the more massive component are as follows: $T_{\text{eff}} = 5314(\pm 42) \text{ K}$, $\log g = 3.78(\pm 0.09) \text{ cm s}^{-2}$, and $[\text{Fe}/\text{H}] = -0.24(\pm 0.04) \text{ dex}$. Finally, the effective temperature of the more massive component was fixed at 5314 K during W-D analysis, while that of the less massive component was adjustable.

Because W UMa-type contact binaries share a CCE, we adopted gravity-darkening coefficients $g_{1,2} = 0.32$ (L. B. Lucy 1967) and bolometric albedos $A_{1,2} = 0.5$ (S. M. Ruciński 1969) for both components. The nonlinear limb-darkening law in the square-root form was adopted, and the bolometric and bandpass limb-darkening coefficients for both components were interpolated from the table provided by Van Hamme (1993). Owing to the contact configuration of V2790 Ori, Mode 3 was selected during the modeling, which is appropriate for over-contact binaries where both component stars filling their Roche lobes. The following parameters are adjustable during the iterations: the orbital semi-major axis a , systemic radial velocity V_γ , orbital inclination i , mass ratio q , the effective temperature of the less massive component, the monochromatic luminosity of the less massive component, and the dimensionless potential of both components $\Omega_1 = \Omega_2$. The contact degree is calculated as $f = (\Omega_{\text{in}} - \Omega)/(\Omega_{\text{in}} - \Omega_{\text{out}}) \times 100\%$. Since the light curves of V2790 Ori exhibit an O’Connell effect, which is commonly attributed to magnetic activity of the components, the spot model was adopted in the W-D analysis. Different spot models were compared during the fitting process, and the optimal solutions were obtained by adding one cool spot on each component separately. The latitude of both spots was fixed at 90° , while other parameters including longitude, angular radius, and temperature factor were adjusted iteratively to reach the final converged solution. Meanwhile, we added the third light (l_3) in the W-D analysis in order to test the possible existence of a third companion. However, the solutions yielded a negative l_3 value, and no convergent solution was obtained.

For clarity and consistency in the subsequent analysis, we redefine the primary component (M_1) as the more massive star and the secondary component (M_2) is the less massive one, so that the adopted mass ratio is less than 1. Finally, the orbital parameters derived from each set of light curves are summarized in Table 2, and the spot parameters are listed in Table A4. The uncertainties of the physical parameters represent the formal errors determined from the W-D program, which are underestimated (e.g., C. Maceroni & S. M. Rucinski 1997; J. Southworth et al. 2007; F. Acerbi et al. 2020; L. Liu 2021). We also analyzed all photometric data simultaneously using the W-D program, and the resulting photometric solution is listed in the "All data" column of Table 2, which is adopted as the final result. The theoretical and observed light curves and radial velocity curve are presented in Figure 1 and Figure 2, respectively.

The absolute physical parameters of V2790 Ori were determined directly through LC program as follows: the semi-major axis $a = 1.92(\pm 0.04) \text{ R}_\odot$, the masses of the two components $M_1 = 0.87(\pm 0.01) \text{ M}_\odot$ and $M_2 = 0.28(\pm 0.01) \text{ M}_\odot$, the radius $R_1 = 0.94(\pm 0.02) \text{ R}_\odot$ and $R_2 = 0.57(\pm 0.01) \text{ R}_\odot$, and the luminosity $L_1 = 0.63(\pm 0.02) \text{ L}_\odot$ and $L_2 = 0.26(\pm 0.01) \text{ L}_\odot$.

4. ORBITAL PERIOD INVESTIGATION

Investigating orbital period variations is an important approach to exploring the evolutionary status and potential companions of contact binaries (e.g., K. Li & S. B. Qian 2013; K. Li et al. 2016, 2019). Such variations are typically analyzed using the $O-C$ method, which represents the difference between the observed and calculated eclipsing minima.

S. A. Otero et al. (2004) first estimated the orbital period for V2790 Ori and derived the initial ephemeris as: $T = 2451521.695(\text{HJD}) + 0.287842 \times E$. To construct a comprehensive $O-C$ diagram and further investigate the orbital period

Table 2. Photometric Solutions for Each Sets of Light Curves of V2790 Ori

| Parameters | 2015 Feb 05 & Mar 06 | 2015 Dec 28 | 2016 Dec 30 | 2017 Dec 20 | 2018 Dec 27 |
|----------------------------------|----------------------------|----------------------------|----------------------|------------------|----------------------|
| $a(R_\odot)$ | 1.89(4) | 1.90(4) | 1.90(4) | 1.89(4) | 1.91(4) |
| $V_\gamma(\text{km/s})$ | -47.91(3) | -47.99(3) | -47.94(3) | -47.81(3) | -48.02(3) |
| q | 0.2923(11) | 0.3082(11) | 0.2908(11) | 0.2784(5) | 0.3165(10) |
| $T_2(K)$ | 5530(6) | 5468(8) | 5418(7) | 5495(5) | 5591(4) |
| $i(^{\circ})$ | 83.0(1) | 84.0(2) | 82.7(2) | 81.6(1) | 84.8(2) |
| $L_{2B}/(L_{1B} + L_{2B})$ | 0.3019(12) | 0.2949(20) | 0.2763(17) | 0.2808(13) | 0.3327(9) |
| $L_{2V}/(L_{1V} + L_{2V})$ | 0.2884(9) | 0.2853(15) | 0.2700(13) | 0.2699(10) | 0.3146(7) |
| $L_{2R_C}/(L_{1R_C} + L_{2R_C})$ | 0.2813(7) | 0.2802(13) | 0.2665(11) | 0.2642(8) | 0.3053(6) |
| $L_{2I_C}/(L_{1I_C} + L_{2I_C})$ | 0.2763(6) | 0.2765(11) | 0.2641(10) | 0.2601(7) | 0.2987(6) |
| r_1 | 0.4953(18) | 0.4887(15) | 0.4912(117) | 0.4940(10) | 0.4867(13) |
| r_2 | 0.2831(5) | 0.2853(4) | 0.2832(4) | 0.2738(3) | 0.2888(3) |
| $f(\%)$ | 11.9(2.9) | 8.4(2.3) | 9.2(2.6) | 1.6(1.3) | 10.5(1.9) |
| Parameters | 2019 Dec 29 & 2020 Jan 03 | 2020 Dec 20 | 2021 Jan 04 & Jan 05 | 2022 Jan 02 | 2022 Dec 31 |
| $a(R_\odot)$ | 1.91(4) | 1.88(4) | 1.92(4) | 1.91(4) | 1.89(4) |
| $V_\gamma(\text{km/s})$ | -48.03(3) | -47.84(3) | -48.04(3) | -48.04(3) | -47.96(3) |
| q | 0.3190(16) | 0.2832(27) | 0.3247(12) | 0.3204(16) | 0.3011(11) |
| $T_2(K)$ | 5652(5) | 5764(10) | 5555(4) | 5637(3) | 5673(4) |
| $i(^{\circ})$ | 85.8(3) | 83.2(3) | 85.0(2) | 86.3(2) | 85.1(2) |
| $L_{2B}/(L_{1B} + L_{2B})$ | 0.3504(14) | 0.3618(24) | 0.3284(10) | 0.3510(11) | 0.3444(10) |
| $L_{2V}/(L_{1V} + L_{2V})$ | 0.3279(12) | 0.3318(19) | 0.3127(8) | 0.3294(9) | 0.3207(8) |
| $L_{2R_C}/(L_{1R_C} + L_{2R_C})$ | 0.3165(11) | 0.3171(18) | 0.3045(8) | 0.3185(9) | 0.3089(7) |
| $L_{2I_C}/(L_{1I_C} + L_{2I_C})$ | 0.3084(11) | 0.3066(17) | 0.2987(7) | 0.3107(8) | 0.3004(7) |
| r_1 | 0.4879(24) | 0.5102(46) | 0.4856(17) | 0.4930(15) | 0.4918(16) |
| r_2 | 0.2892(6) | 0.2931(11) | 0.2909(4) | 0.2972(4) | 0.2855(4) |
| $f(\%)$ | 10.8(3.5) | 32.4(6.8) | 11.0(2.4) | 22.9(2.2) | 11.7(2.4) |
| Parameters | 2024 Feb 27 & Mar 08 | 2025 Jan 08 | 2015 Jan 08 – 29 | 2015 Nov 19 & 20 | 2020 Jan 29 – Feb 05 |
| $a(R_\odot)$ | 1.91(4) | 1.90(4) | 1.90(4) | 1.89(4) | 1.90(4) |
| $V_\gamma(\text{km/s})$ | -48.01(3) | -47.96(3) | -47.94(3) | -47.89(3) | -47.92(3) |
| q | 0.3077(18) | 0.3000(5) | 0.2982(6) | 0.2982(6) | 0.2900(4) |
| $T_2(K)$ | 5523(8) | 5471(6) | 5505(6) | 5477(6) | 5487(5) |
| $i(^{\circ})$ | 83.0(2) | 83.8(1) | 82.6(2) | 82.2(2) | 82.0(1) |
| $L_{2B}/(L_{1B} + L_{2B})$ | 0.3107(15) | 0.2902(14) | 0.2971(14) | 0.2837(15) | — |
| $L_{2V}/(L_{1V} + L_{2V})$ | 0.2974(11) | 0.2805(11) | 0.2852(10) | 0.2737(11) | — |
| $L_{2R_C}/(L_{1R_C} + L_{2R_C})$ | 0.2904(10) | 0.2753(9) | — | — | — |
| $L_{2I_C}/(L_{1I_C} + L_{2I_C})$ | 0.2855(9) | 0.2717(8) | — | 0.2648(8) | — |
| $L_{2g'}/(L_{1g'} + L_{2g'})$ | — | — | — | — | 0.2856(10) |
| $L_{2r'}/(L_{1r'} + L_{2r'})$ | — | — | — | — | 0.2709(6) |
| $L_{2i'}/(L_{1i'} + L_{2i'})$ | — | — | — | — | 0.2751(7) |
| r_1 | 0.4925(28) | 0.4903(7) | 0.4893(9) | 0.4905(12) | 0.4917(6) |
| r_2 | 0.2887(9) | 0.2823(3) | 0.2805(4) | 0.2766(4) | 0.2810(2) |
| $f(\%)$ | 15.0(4.3) | 6.9(1.2) | 4.1(1.5) | 1.1(1.9) | 7.2(0.9) |
| Parameters | TESS – S43 | TESS – S44 | TESS – S45 | TESS – S71 | TESS – S72 |
| $a(R_\odot)$ | 1.93(4) | 1.90(4) | 1.91(4) | 1.92(4) | 1.91(4) |
| $V_\gamma(\text{km/s})$ | -48.06(3) | -48.00(3) | -48.03(3) | -48.06(3) | -48.05(3) |
| q | 0.3342(12) | 0.3083(4) | 0.3182(5) | 0.3276(11) | 0.3266(9) |
| $T_2(K)$ | 5651(4) | 5641(2) | 5621(2) | 5794(4) | 5746(3) |
| $i(^{\circ})$ | 86.0(2) | 84.5(1) | 84.8(1) | 88.3(2) | 88.3(2) |
| $L_{2T}/(L_{1T} + L_{2T})$ | 0.3208(6) | 0.3047(3) | 0.3067(3) | 0.3374(7) | 0.3301(6) |
| r_1 | 0.4876(16) | 0.4950(5) | 0.4905(7) | 0.4899(14) | 0.4908(13) |
| r_2 | 0.2978(3) | 0.2930(1) | 0.2933(2) | 0.2983(3) | 0.2976(3) |
| $f(\%)$ | 18.5(2.2) | 21.3(0.7) | 17.3(1.1) | 21.5(2.0) | 21.2(1.8) |
| Parameters | TNO – 2015 Jan 21 – Jan 23 | KAO – 2017 Jan 21 & Jan 22 | All data | | |
| $a(R_\odot)$ | 1.90(4) | 1.93(4) | 1.92(4) | | |
| $V_\gamma(\text{km/s})$ | -47.99(3) | -48.06(3) | -48.03(3) | | |
| q | 0.3056(7) | 0.3313(20) | 0.3221(3) | | |
| $T_2(K)$ | 5440(8) | 5393(7) | 5489(2) | | |
| $i(^{\circ})$ | 83.0(1) | 85.5(3) | 84.5(1) | | |
| $L_{2B}/(L_{1B} + L_{2B})$ | 0.2856(21) | — | 0.3105(6) | | |
| $L_{2V}/(L_{1V} + L_{2V})$ | 0.2779(16) | 0.2868(14) | 0.2993(4) | | |
| $L_{2R_C}/(L_{1R_C} + L_{2R_C})$ | 0.2737(13) | 0.2840(12) | 0.2934(4) | | |
| $L_{2I_C}/(L_{1I_C} + L_{2I_C})$ | — | 0.2821(11) | 0.2892(3) | | |
| $L_{2g'}/(L_{1g'} + L_{2g'})$ | — | — | 0.3054(5) | | |
| $L_{2r'}/(L_{1r'} + L_{2r'})$ | — | — | 0.2943(4) | | |
| $L_{2i'}/(L_{1i'} + L_{2i'})$ | — | — | 0.2899(3) | | |
| $L_{2T}/(L_{1T} + L_{2T})$ | — | — | 0.2898(3) | | |
| r_1 | 0.4879(11) | 0.4863(24) | 0.4861(2) | | |
| r_2 | 0.2840(4) | 0.2971(6) | 0.2928(4) | | |
| $f(\%)$ | 7.0(1.7) | 18.3(3.3) | 14.8(0.6) | | |

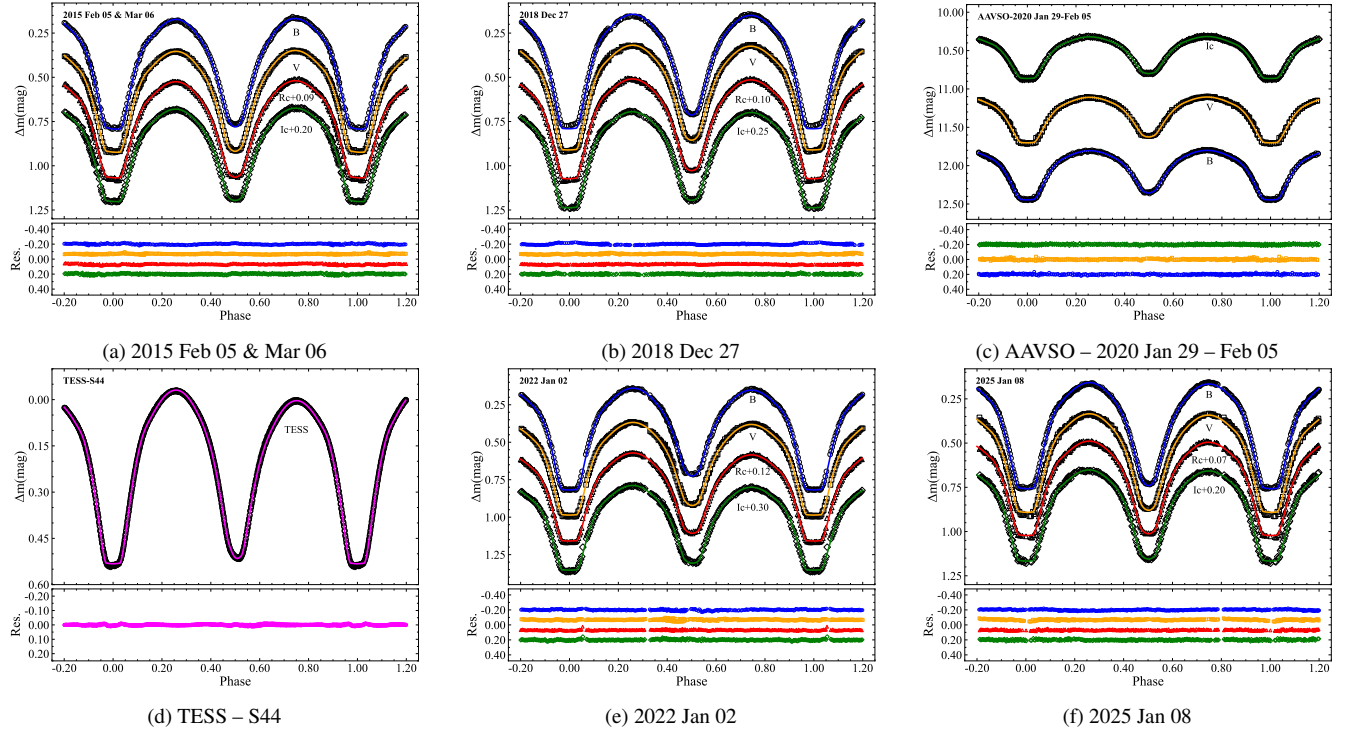


Figure 1. Theoretical light curves (solid lines) fitted by W-D program compared to observed ones for V2790 Ori. The fitted residuals are displayed at the bottom of each panel. All figures of 22 sets of light curves are available in the online journal.

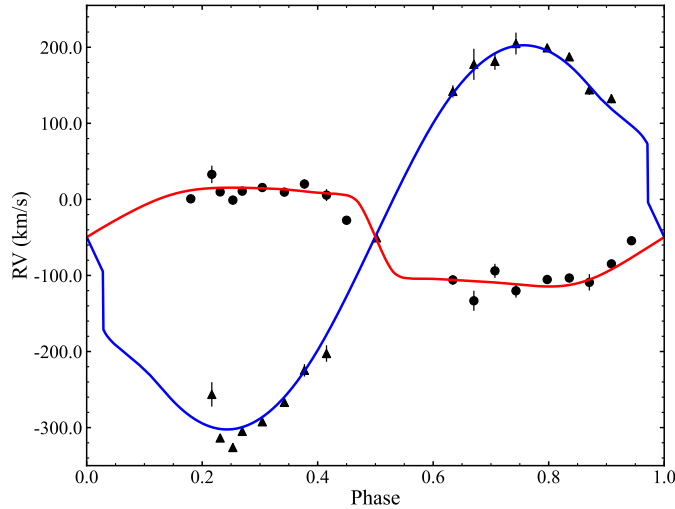


Figure 2. Radial velocity and fitted curves of V2790 Ori. The black triangular represents the radial velocity of the less massive component, and the black circular represents the radial velocity of the more massive component. The blue lines show the theoretical curves of the less massive components, and the red lines show the theoretical curves of the more massive components.

variations of V2790 Ori, we collected as many eclipsing minima as possible. In total, 445 minima spanning nearly 25 years were used in our analysis, including 31 from our photometric observations, 23 from AAVSO, 4 from Brno Regional Network of Observers project⁵ (BRNO), 359 from TESS, 2 from the All-Sky Automated Survey for SuperNovae (ASAS-SN; B. J. Shappee et al. 2014; T. Jayasinghe et al. 2019), and 26 from other literatures. The K-W method (K. K. Kwee & H. van Woerden 1956) was

⁵ <http://var2.astro.cz/EN/brno/index.php>

used to calculate the eclipsing minima, except for those from other literatures. Since the observations of ASAS-SN and TESS at a 10-minute cadence are dispersed, we applied the phase shift method proposed by [K. Li et al. \(2020, 2021a,b\)](#) to compute eclipsing minima for these data. Because the minima of TESS data are given in Barycentric Julian Date (BJD), all other eclipsing minima were converted to BJD using the OSU Online Astronomy Utilities⁶ provided by [J. Eastman et al. \(2010\)](#). The following ephemeris was adopted to calculate the $O - C$ values:

$$T = 2458480.26150 \text{ (BJD)} + 0.287842 \times E, \quad (2)$$

where T denotes the theoretical BJD corresponding to E cycles. The initial epoch BJD 2458480.26150 is from our observation on 2018 December 27. A linear least-squares fit to all minima yields the updated ephemeris:

$$T = 2458480.26187(\pm 0.000006) \text{ (BJD)} + 0.28784126(\pm 0.00000002) \times E. \quad (3)$$

Using this new ephemeris, we recalculated the $O - C$ values (denoted as $(O - C)_1$), which are listed in Table A5. The corresponding $(O - C)_1$ curves are shown in the upper panel of Figure 3.

As shown in Figure 3, the $(O - C)_1$ curves exhibits a trend of periodic variation. This phenomenon can be interpreted either as the light-travel time effect (LTTE; [J. Woltjer 1922](#); [J. B. Irwin 1959](#)) caused by a third body or as the magnetic activity cycle ([J. H. Applegate 1992](#)). We employed two models to fit the $(O - C)_1$ curves: (i) a quadratic-plus-sinusoid model (Q+S) and (ii) a quadratic-plus-LTTE model (Q+L), where LTTE corresponds to the five-parameter-LTTE solution described by [J. B. Irwin \(1952\)](#). The two models are expressed as:

$$(O - C)_1 = \Delta T_0 + \Delta P_0 \times E + \frac{\beta}{2} \times E^2 + A \times \sin\left(\frac{2\pi}{P_3} \times E + \varphi\right), \quad (4)$$

$$(O - C)_1 = \Delta T_0 + \Delta P_0 \times E + \frac{\beta}{2} \times E^2 + A \times \left[\sqrt{1 - e^2} \sin E^* \cos \omega + \cos E^* \sin \omega \right], \quad (5)$$

Where ΔT_0 and ΔP_0 are the corrections of T_0 and P_0 , respectively. The parameter β denotes the secular change rate of the period, and A and P_3 are the semi-amplitude and period of the periodic term. The parameters e , ω , and E^* denote the eccentricity, longitude of periastron, and eccentric anomaly of the third body's orbit, respectively ([J. B. Irwin 1952](#)). In fact, when the eccentricity $e = 0$, the LTTE model reduces to a sinusoidal form given in Equation (4). The Levenberg-Marquardt algorithm was employed to fit the $(O - C)_1$ curve of Q+L model. The final fitting curves are presented in Figure 3, and the fitted parameters from both models are listed in Table 3.

To determine the preferred model, we calculated the residual sum of squares (RSS) for both models and employed the Akaike Information Criterion (AIC) and Bayes Information Criterion (BIC). The results of RSS, AIC, and BIC are summarized in Table 3. By comparing these values, the RSS, AIC and BIC of Q+S model is smaller, suggesting that it offers a superior fit to the data. Based on this model, the orbital period is decreasing at a rate of $\dot{P} = -3.18(\pm 0.75) \times 10^{-8} \text{ d yr}^{-1}$, accompanied by a periodic variation with an amplitude of $A = 8.98(\pm 2.19) \times 10^{-4}$ days and a period of $P_3 = 7.44(\pm 0.52) \text{ yr}$.

5. DISCUSSIONS AND CONCLUSIONS

From the spectroscopic and decade-long multiband photometric observations of V2790 Ori, we derived its physical parameters through a simultaneous analysis of the light and radial velocity curves using the W-D program. The criteria for classifying contact binaries as deep, medium, or shallow are as follows: $f \geq 50\%$ is deep, $25\% \leq f < 50\%$ is medium, and $f < 25\%$ is shallow ([S.-B. Qian et al. 2005](#); [K. Li et al. 2022](#); [X.-Y. Liu et al. 2023](#)). Therefore, V2790 Ori is a W-subtype shallow contact binary with a mass ratio of $q = 0.322(\pm 0.001)$ and a contact degree of $14.8(\pm 0.6)\%$, which is generally consistent with the results of previous studies as shown in Table A1. Based on the effective temperatures of both components, the spectral type of the primary component is estimated to be G9 and that of the secondary G7 ([M. J. Pecaut & E. E. Mamajek 2013](#)).

5.1. Orbital Period Variations and Their Physical Origins

[W. Kriwattanawong & K. Kriwattanawong \(2019\)](#) and [K. B. Alton & K. Stępień \(2021\)](#) have previously investigated the orbital period variations of V2790 Ori, as summarized in Table A1. [W. Kriwattanawong & K. Kriwattanawong \(2019\)](#) reported an orbital period increase based on 36 eclipsing minima spanning nearly 12 years, attributing it to mass transfer from the less

⁶ <http://astroutils.astronomy.ohio-state.edu/time/>

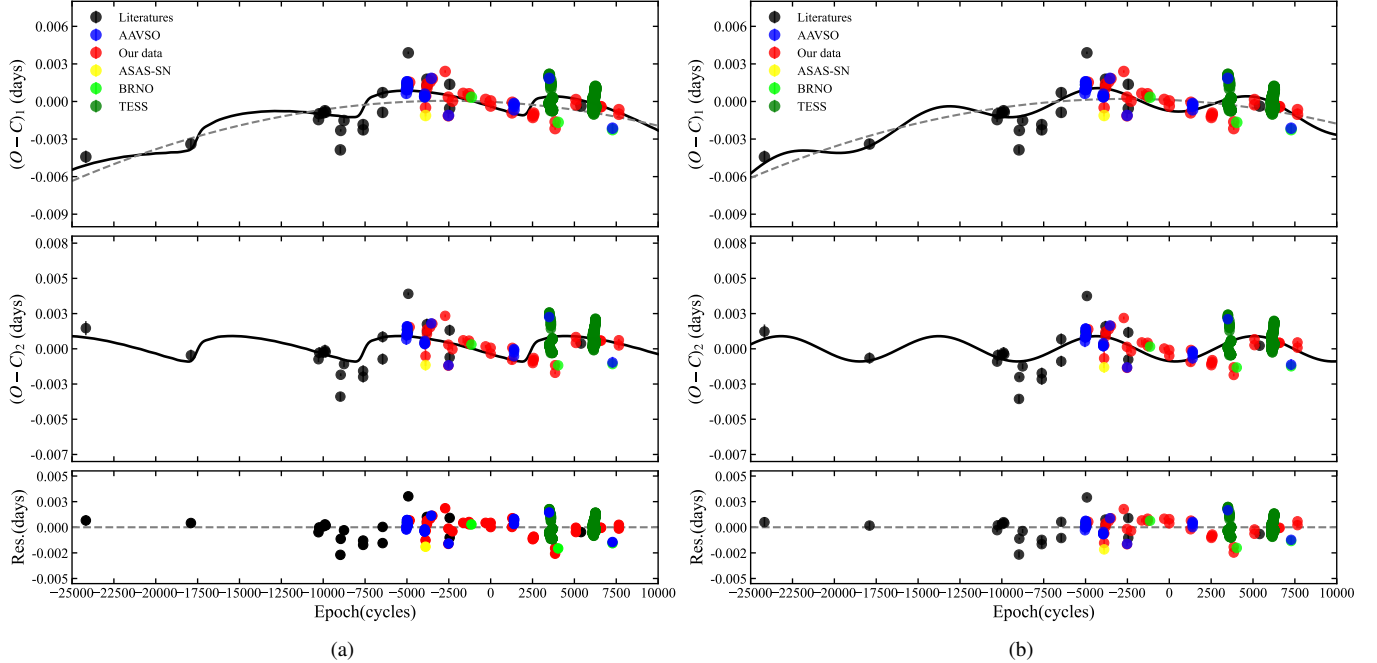


Figure 3. $O - C$ curves of V2790 Ori. (a) Fitting result of Q+L model. (b) Fitting result of Q+S model. The top panel shows the $(O - C)_1$ curve determined by the new linear ephemeris of Equation (3). The $(O - C)_2$ values, which remove the quadratic term from the $(O - C)_1$ curve, are plotted in the middle panel. The residuals from the full ephemeris of Equation (4) or (5) are displayed in the lower panel.

Table 3. Fitting Results of Two Models for $O - C$

| Parameter | Q+S | Q+L |
|---------------------------|----------------------------------|-----------------------------------|
| ΔT_0 (days) | $1.25(\pm 1.80) \times 10^{-4}$ | $-2.65(\pm 26.33) \times 10^{-5}$ |
| ΔP_0 | $-6.44(\pm 2.34) \times 10^{-8}$ | $-6.42(\pm 1.22) \times 10^{-8}$ |
| \dot{P} (d yr $^{-1}$) | $-3.18(\pm 0.75) \times 10^{-8}$ | $-3.22(\pm 0.32) \times 10^{-8}$ |
| A (days) | $8.98(\pm 2.19) \times 10^{-4}$ | $1.74(\pm 4.42) \times 10^{-3}$ |
| e | — | $0.888(\pm 0.611)$ |
| ω (°) | — | $6.00(\pm 0.64)$ |
| P_3 (yr) | $7.44(\pm 0.52)$ | $8.05(\pm 1.26)$ |
| T_3 | — | $2453517(\pm 10561)$ |
| ϕ (°) | $256.26(\pm 11.01)$ | — |
| RSS | 0.000245 | 0.000248 |
| AIC | -6401.5 | -6392.1 |
| BIC | -6376.9 | -6359.3 |

massive component to the more massive component. Earlier, E. J. Michaels (2016) had detected a small cyclic change but lacked enough data to perform the necessary calculations. More recently, K. B. Alton & K. Stępień (2021) found a period decrease superimposed with a cyclic variation based on eclipsing minima covering about 20 years, which was interpreted as the LTTE induced by a third body. In this study, we collected 445 eclipsing minima spanning nearly 25 years. Our analysis shows that the orbital period of V2790 Ori is undergoing a secular decrease at a rate of $\dot{P} = -3.18(\pm 0.75) \times 10^{-8}$ d yr $^{-1}$, superimposed with a cyclic variation with an amplitude of $A = 8.98(\pm 2.19) \times 10^{-4}$ d and a period of $P_3 = 7.44(\pm 0.52)$ yr.

5.1.1. Secular Period Decrease

In general, the continuous orbital period decrease can be attributed to AML and mass transfer from the more massive component to the less massive one. Stellar wind-driven magnetic braking can substantially contribute to the AML process. Based on the magnetic braking model (E. J. Weber & L. Davis 1967), E. F. Guinan & D. H. Bradstreet (1988) derived the orbital period decrease rate as follows:

$$\dot{P}_{\text{aml}} \approx -1.1 \times 10^{-8} \times \frac{(1+q)^2}{q} \times \frac{k_1^2 M_1 R_1^4 + k_2^2 M_2 R_2^4}{(M_1 + M_2)^{5/3} P^{7/3}}, \quad (6)$$

where k_1 and k_2 are the gyration radius of the primary and secondary components, respectively. During the calculations, k_1 was determined using the relations derived by N. R. Landin et al. (2009): $k_1 = 0.5391 - 0.2504 \times M_1$ ($0.4M_{\odot} < M_1 < 1.4M_{\odot}$), where both the rotation and tidal distortions of the two components were taken into account. Because the mass of the secondary component is very low, it should be a fully convective star, $k_2^2 = 0.205$ was used (B. Arbutina 2007). By substituting the physical parameters into Equation (6), the period decrease rate due to AML was calculated to be $\dot{P}_{\text{aml}} = -6.57 \times 10^{-8} \text{ d yr}^{-1}$. This value is close to the observed rate of $\dot{P} = -3.18(\pm 0.75) \times 10^{-8} \text{ d yr}^{-1}$, suggesting that the AML is sufficient to account for the secular decrease of orbital period. Assuming the conservation of mass and angular momentum, the mass transfer rate can be estimated using the following relation (J. E. Pringle 1975):

$$\dot{M}_1 = -\dot{M}_2 = \frac{M_1 M_2}{3P(M_1 - M_2)} \times \dot{P}. \quad (7)$$

Accordingly, the mass transfer rate from the primary to the secondary component is calculated to be $\dot{M}_1 = -1.22(\pm 0.29) \times 10^{-8} M_{\odot} \text{ yr}^{-1}$.

5.1.2. Cyclic Period Variation

As shown in the middle panel of Figure 3, the $(O - C)_2$ curve exhibits a clear cyclic variation. Such cyclic variation observed in the orbital period of eclipsing binaries are commonly explained by the LTTE caused by a third body (e.g., K. Li et al. 2014, 2018; X. Zhou 2025; B. Zhang et al. 2025) or the magnetic activity cycle of one or both components (J. H. Applegate 1992). According to statistical analysis, W UMa-type contact binaries have a high probability to belong to multiple systems (W. P. Liao & S. B. Qian 2010; C. R. Chambliss 1992). Therefore, assuming that the cyclic variation in the orbital period of V2790 Ori is caused by a third body, the projected distance between the eclipsing binary and the barycenter of the triple system is given by $a_{12} \sin i_3 = A \times c$, where a_{12} is the orbital radius of the binary around the center of mass of the triple system, i_3 is the inclination of the third body's orbit, and c is the speed of light. By inserting the amplitude and period of the cyclic variation, $a_{12} \sin i_3$ is computed to be $0.16(\pm 0.04)$ AU. Using the following equation:

$$f(M_3) = \frac{4\pi}{GP_3^2} \times (a_{12} \sin i_3)^3 = \frac{(M_3 \sin i_3)^3}{(M_1 + M_2 + M_3)^2}, \quad (8)$$

the mass function of the third body was calculated as $f(M_3) = 6.80(\pm 4.98) \times 10^{-4} M_{\odot}$. The orbital distance between the third body and the inner binary can be estimated using $a_3 = (M_1 + M_2) \times a_{12} / M_3$. Assuming a coplanar orbit ($i_3 = i = 84^{\circ}.5$), the mass of the third body is determined to be $M_3 = 0.046 \pm 0.019 M_{\odot}$, and the corresponding orbital distance is $a_3 = 4.57 \pm 2.21$ AU. This suggests that the third component is a brown dwarf, whose upper mass limit is approximately $0.072 M_{\odot}$ (G. Basri & A. J. Burgasser 2023).

Applegate's theory (J. H. Applegate 1992) proposes that magnetic activity cycle in a binary system can drive cyclic variation in the orbital period by inducing internal structural variations, which are coupled to the orbit via tidal interactions. Both the photometric solutions and the variable O'Connell effect are indicative of the magnetic activity in V2790 Ori. If the magnetic activity mimics the variation in the orbital period and results in the observed cyclic variation, the required variation of the gravitational quadrupole moment ΔQ can be determined using the following equation (A. F. Lanza & M. Rodonò 2002):

$$\frac{\Delta P}{P} = \frac{2\pi \times A}{P_3} = -9 \frac{\Delta Q}{Ma^2}, \quad (9)$$

where ΔP is the period of cyclic variation, P is the orbital period, M , R , and a denote the mass, radius of the magnetically active components, and the semi-major axis of the binary system, respectively. Based on this relation, we derived $\Delta Q_1 = 7.07 \times 10^{48} \text{ g cm}^2$ and $\Delta Q_2 = 2.30 \times 10^{48} \text{ g cm}^2$ for the primary and secondary components. However, under the assumption of angular momentum conservation, the typical value of ΔQ is on the order of $10^{51}\text{--}10^{52} \text{ g cm}^2$ for close binaries and 10^{49} g cm^2 for

the cataclysmic variables (A. F. Lanza & M. Rodonò 1999). The values of ΔQ_1 and ΔQ_2 obtained for V2790 Ori are significantly lower than these typical ranges, suggesting that the Applegate mechanism cannot adequately explain the cyclic period variation observed in this system. Therefore, such variation can be attributed to the LTTE caused by a third body, which is a brown dwarf. It is worth noting that no third light has been detected in either our analysis or previous studies of V2790 Ori (E. J. Michaels 2016; K. B. Alton & K. Stępień 2021), or it may be too faint to be identified through LC modeling, which is consistent with the presence of a brown dwarf companion.

5.2. O'Connell effect variation

Given the interpretation of the O'Connell effect as being caused by active spots, it may serve as a reliable indicator of magnetic activity. Theoretically, the period of magnetic activity cycle should be consistent with the variation period of the O'Connell effect. In the case of V2790 Ori, the different spot solutions from our (Table A4) and previous studies (Table A1), together with the 22 sets of light curves presented in Figure 1 that exhibit variable O'Connell effect, enable the investigation of a potential magnetic activity cycle.

In order to quantify the O'Connell effect, we first calculated the magnitude difference between the primary and secondary maxima (Δm) in each light curve, which is a conventional metric. In addition to this basic measurement, we also employed the O'Connell effect ratio (OER), as proposed by S. McCartney (1997). OER is defined as the ratio of the areas beneath the two maxima of a phase-folded light curve. For the numerical analysis, the phase-folded light curve is initially divided into n equal-width phase bins, with n chosen to ensure adequate sampling of the light curve. The average magnitude within each bin is then computed and normalized by subtracting the mean magnitude of the bin corresponding to the primary minimum. The OER is finally calculated using the following equation:

$$OER = \frac{\sum_{k=1}^{n/2} (m_k - m_1)}{\sum_{k=n/2+1}^n (m_k - m_1)}, \quad (10)$$

where m_k denotes the mean magnitude in the k th bin. Compared to the conventional Δm measurement, the OER provides a more sensitive diagnostic for detecting asymmetries in the out-of-eclipse regions of a light curve. Notably, it has been proven to be more valuable for tracing the continuous variation of light-curve asymmetry over time (N. J. Wilsey & M. M. Beaky 2009), and has been adopted in numerous studies (e.g., K. Hu et al. 2020; M. F. Knot 2021; Z.-B. Meng et al. 2024).

Using the 22 available light curves, we calculated both Δm and OER values of all bands, with results summarized in Table A6. To ensure consistency in investigating the long-term variation of the O'Connell, we selected the V band for most light curves, the g' band for one AAVSO light curve, and the TESS band for 5 light curves from TESS. To search for the cyclic variation in the O'Connell effect, we fitted both Δm and OER data using the following sinusoidal function:

$$f(x) = a + A_m \times \sin\left(\frac{2\pi}{P_m} \times E + \varphi\right), \quad (11)$$

where A_m , P_m , and φ represent the amplitude, period and initial phase of the sine term, respectively. E denotes the cycle number, consistent with our previous definition. Through least-squares fitting, we obtained the following final expressions:

$$\Delta m = 0.01332(\pm 0.01137) + 0.03245(\pm 0.01502) \times \sin\left(\frac{2\pi}{5.43(\pm 0.68)} \times E - 212.28(\pm 26.65)\right), \quad (12)$$

$$OER = 1.02547(\pm 0.00272) + 0.08589(\pm 0.03611) \times \sin\left(\frac{2\pi}{5.46(\pm 0.61)} \times E - 214.75(\pm 23.67)\right), \quad (13)$$

and the fitting curves are presented in Figure 4. The derived periods of variation in Δm and OER are $5.43(\pm 0.68)$ yr and $5.46(\pm 0.61)$ yr, respectively. This indicates that V2790 Ori likely exhibits a solar-like magnetic activity cycle with a period of approximately 5.4 years. The period of the observed cyclic period variation ($P_3 = 7.44(\pm 0.52)$ yr) differs from that of the magnetic activity cycle, which further confirms that the magnetic activity cycle is insufficient to explain the cyclic period variation. To further confirm this magnetic activity cycle, more observations in the future are required for verification.

5.3. Evolutionary State

In order to further investigate the evolutionary status of both components, the mass-radius and the mass-luminosity diagrams were constructed based on the absolute physical parameters of V2790 Ori as shown in Figure 5. Although no reliable evolutionary

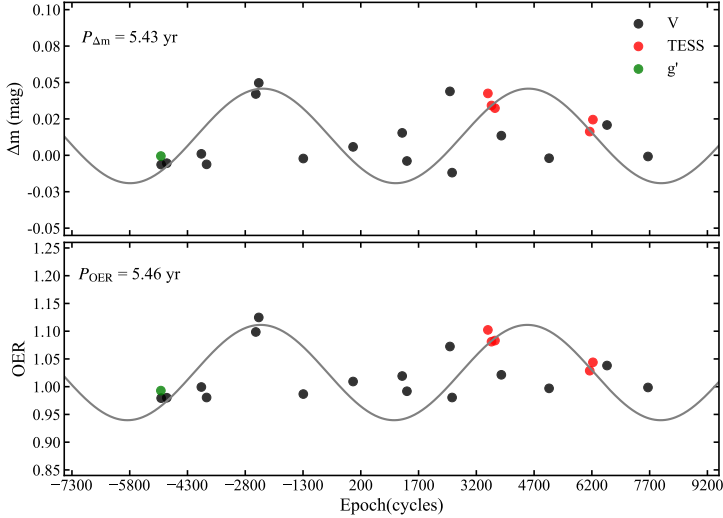


Figure 4. Possible cyclic variations for Δm and OER. The solid lines represent the sinusoidal fit with Equation (12) and Equation (13). The periods determined are presented in the top left corner of each panel.

model has been established for contact systems, the zero-age and terminal-age main sequence (ZAMS and TAMS) lines adopted in our analysis were derived from the binary star evolution code of J. R. Hurley et al. (2002). As shown in Figure 5, V2790 Ori lies within the distribution region of W-subtype contact binaries, where the primary component is located between the ZAMS and TAMS lines, whereas the secondary component is above the TAMS line. This implies that the primary component is still on the main sequence, while the secondary component has evolved off the main sequence and appears oversized and over-luminous compared to a main-sequence star of the same mass. This may be attributed to energy and mass transfer from the primary to the secondary component during the early evolutionary stages of the system.

The orbital angular momentum J_{orb} of V2790 Ori was calculated using the following equation from P. E. Christopoulou & A. Papageorgiou (2013):

$$J_{\text{orb}} = 1.24 \times 10^{52} \times M_{\text{T}}^{3/5} \times P^{1/3} \times q \times (1+q)^{-2}, \quad (14)$$

where q is the mass ratio, $M_{\text{T}} = M_1 + M_2$ is the total mass of the binary system, and P is the orbital period. The orbital angular momentum of V2790 Ori is computed to be $\log J_{\text{orb}} = 51.2$ cgs. Then the diagram of M_{T} versus J_{orb} is shown in Figure 5, and the position of V2790 Ori is located below and near the boundary line. In combination with the shallow contact degree of V2790 Ori, this suggests that the system is a newly formed contact binary. Moreover, its current orbital angular momentum is lower than that of detached systems with the same total mass, supporting the interpretation that angular momentum and mass loss during the earlier detached phase led the binary to evolve into contact configuration.

The progenitors of both components of V2790 Ori were estimated using the following equations from M. Yıldız & T. Doğan (2013):

$$M_{\text{Si}} = M_{\text{S}} + \Delta M, \quad (15)$$

$$M_{\text{Pi}} = M_{\text{P}} - (\Delta M - M_{\text{lost}}) = M_{\text{P}} - \Delta M(1 - \gamma), \quad (16)$$

$$\Delta M = 2.50 \times \left[\left(\frac{L_{\text{S}}}{1.49} \right)^{1/4.216} - M_{\text{S}} - 0.07 \right]^{0.64}, \quad (17)$$

where M_{Pi} and M_{Si} are the initial masses, and M_{P} and M_{S} are the current masses of the primary and secondary components, respectively. L_{S} is the luminosity of the secondary component. ΔM is defined as the total mass lost by the secondary component, M_{lost} refers to the mass lost from the system, and γ is the ratio $M_{\text{lost}}/\Delta M$. Using the observed values of $M_{\text{S}} = 0.282 \pm 0.013 M_{\odot}$ and $L_{\text{S}} = 0.262 \pm 0.012 L_{\odot}$, the initial mass of the secondary component is calculated as $1.465 \pm 0.048 M_{\odot}$, and the total mass lost by the secondary is $1.183 \pm 0.035 M_{\odot}$. M. Yıldız & T. Doğan (2013) suggested that the value of γ for W-subtype contact binaries lies within the range 0.500-0.664, and Figure A2 shows the relation between present total mass M_{T} and initial total mass M_{Ti} for A-subtype and W-subtype contact binaries from M. Yıldız (2014). The positions of V2790 Ori corresponding to the two boundary γ values are marked with a red solid hexagon and a red solid triangle, respectively. As shown in Figure A2,

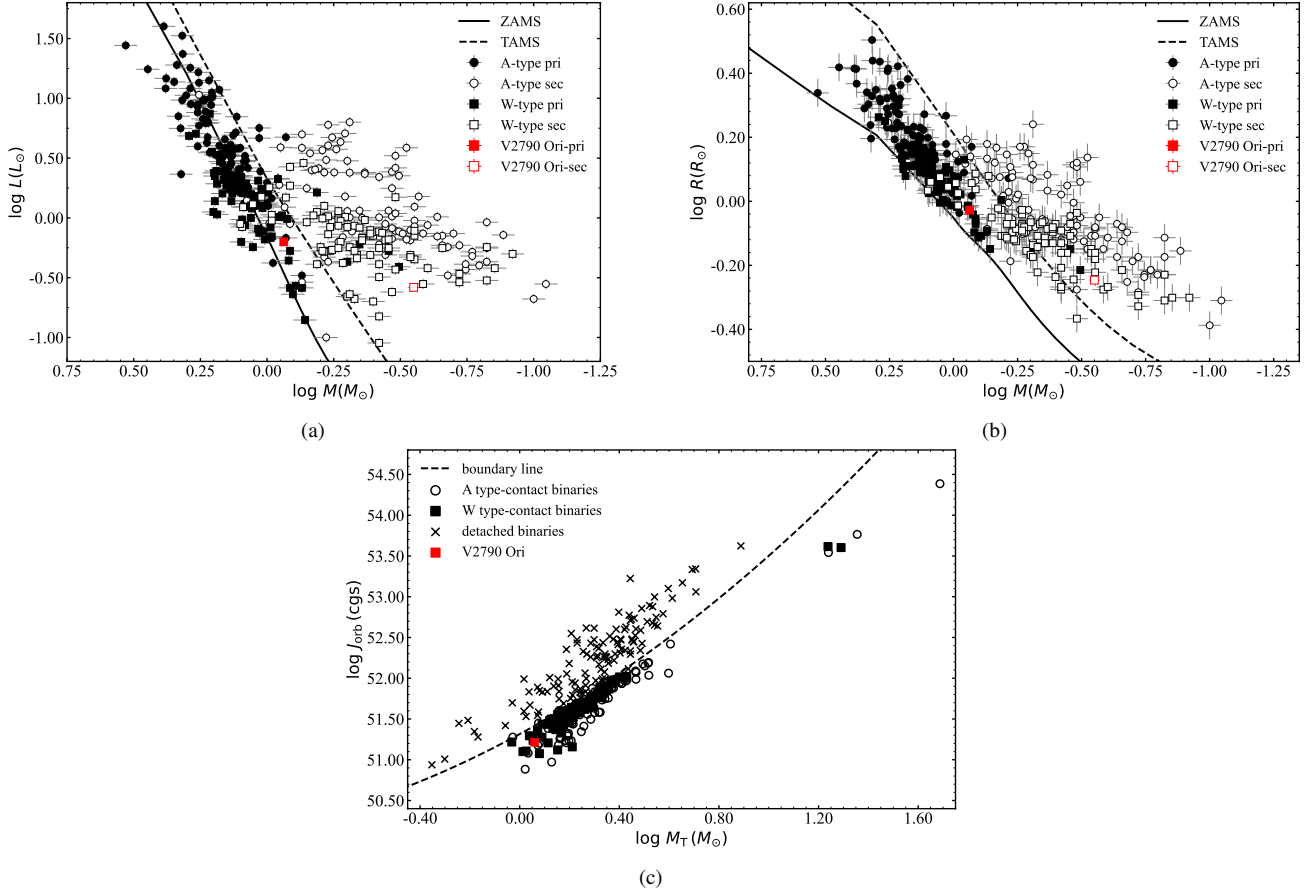


Figure 5. (a) The relation of M-L. (b) The relation of M-R. The zero-age main sequence (ZAMS) and terminal-age main sequence (TAMS), generated using the binary star evolution code from J. R. Hurley et al. (2002), are plotted as solid and dashed black lines, respectively. Circular and square symbols represent W-subtype and A-subtype contact binaries, respectively, and are taken from K. Li et al. (2021b). Solid symbols denote the more massive primary components, while open symbols represent the less massive secondary components. The positions of the components of V2790 Ori are marked with red squares. (c) The relation between orbital angular momentum and total mass for detached and contact binaries. The dashed boundary line between detached and contact binaries and detached binaries are adopted from Z. Eker et al. (2006). The samples of contact binaries are taken from K. Li et al. (2021b). Open circular and solid square symbols represent A-subtype and W-subtype contact binaries, respectively. The position of V2790 Ori is marked with a red solid square.

the case where $\gamma = 0.664$ lies closer to the fitted line for W-subtype systems. Thus, the appropriate value of γ for V2790 Ori should be 0.664. So the initial mass of the primary component is determined as $M_{\text{Pi}} = 0.468(\pm 0.008) M_{\odot}$. Initially, V2790 Ori was in a detached configuration. The more massive progenitor of the current secondary component evolved more rapidly toward TAMS and filled its Roche lobe first, which led to the beginning of mass transfer. The progenitor of the secondary component transferred $0.397 \pm 0.012 M_{\odot}$ to the progenitor of the primary component, resulting in a reversal of the mass ratio. Meanwhile, a total of $0.785(\pm 0.024) M_{\odot}$ has been lost from the system since the detached phase. Eventually, the system evolved into the current W-subtype contact binary system. Additionally, K. B. Alton & K. Stępień (2021) suggested that the initial orbital period of V2790 Ori lies in the range of 2-4 days, corresponding to the peak of the orbital period distribution predicted by the influence of Kozai cycles (Y. Kozai 1962) coupled with tidal friction (D. Fabrycky & S. Tremaine 2007), under the assumption that the system contains a third body (P. P. Eggleton & L. Kisselava-Eggleton 2006; S. M. Rucinski et al. 2007). This further proves that the observed cyclic variation in the orbital period is caused by a third body.

In summary, we conducted spectroscopic and decade-long photometric observations of V2790 Ori. The physical parameters of the system were determined through a simultaneous analysis of its light curves and radial velocity curve. The orbital period was investigated using 445 eclipsing times, revealing a secular decrease superimposed with a cyclic variation. The secular decrease is attributed to AML, while the periodic variation, with a period of $P_3 = 7.44(\pm 0.52)$ years, is explained by the LTTE induced by third body, which is most likely to be a brown dwarf. Based on the long-term variation of the O'Connell effect, a solar-like

magnetic activity cycle with a period of approximately 5.4 years was identified through the analysis of Δm and OER using all available light curves. Evolutionary analysis suggests that V2790 Ori is a newly formed W-subtype contact binary system, which has evolved from a detached phase into the present contact configuration via a combination of mass transfer, mass loss, and AML. Therefore, in order to robustly confirm the magnetic activity cycle and orbital period variations of V2790 Ori, continuous photometric observations will be essential in the future.

ACKNOWLEDGMENTS

We are grateful to the anonymous referee for the constructive comments and valuable suggestions that significantly improved this manuscript. This work is supported by the National Natural Science Foundation of China (NSFC, No. 12273018), the Joint Research Fund in Astronomy (No. U1931103) under a cooperative agreement between NSFC and the Chinese Academy of Sciences (CAS), the Taishan Scholars Young Expert Program of Shandong Province, the Qilu Young Researcher Project of Shandong University, and the Young Data Scientist Project of the National Astronomical Data Center. The calculations in this work were carried out at Supercomputing Center of Shandong University, Weihai.

We acknowledge the support of the staff of the Xinglong 85 cm, 2.16 m telescopes, NEXT and WHOT. This work was partially supported by National Astronomical Observatories, Chinese Academy of Sciences.

This work includes data collected by the TESS mission. Funding for the TESS mission is provided by NASA Science Mission Directorate. The specific observations analyzed in this work can be accessed via the MAST at DOI: [10.17909/fwdt-2x66](https://doi.org/10.17909/fwdt-2x66). We acknowledge the TESS team for its support of this work. We gratefully acknowledge the variable star observations from the AAVSO International Database, contributed by observers worldwide and used in this research. We also appreciate the observers around the world for providing the BRNO data of V2790 Ori. We thank Las Cumbres Observatory and its staff for their continued support of ASAS-SN. ASAS-SN is funded in part by the Gordon and Betty Moore Foundation through grants GBMF5490 and GBMF10501 to the Ohio State University, and also funded in part by the Alfred P. Sloan Foundation grant G2021-14192. This work has made use of data from the European Space Agency (ESA) mission Gaia (<https://www.cosmos.esa.int/gaia>), processed by the Gaia Data Processing and Analysis Consortium (DPAC; <https://www.cosmos.esa.int/web/gaia/dpac/consortium>). Funding for the DPAC has been provided by national institutions, in particular the institutions participating in the Gaia Multilateral Agreement.

APPENDIX

M. Gull et al. (2025) This Appendix provides supplementary tables and figures for V2790 Ori. Table A2 presents the photometric data of V2790 Ori. Figure A1 displays the spectra of BFOSC near phase 0. Table A3 provides the radial velocities of V2790 Ori. Table A4 lists the spot parameters of V2790 Ori. Figure A2 shows the relation between present total mass and initial total mass. Table A5 gives the eclipsing minima of V2790 Ori. All calculated measurements of the O’Connell effect in the light curves of V2790 Ori are summarized in Table A6.

REFERENCES

Acerbi, F., Michel, R., Barani, C., Martignoni, M., & Fox-Machado, L. 2020, Research in Astronomy and Astrophysics, 20, 062, doi: [10.1088/1674-4527/20/4/62](https://doi.org/10.1088/1674-4527/20/4/62)

Alton, K. B., & Stępień, K. 2021, AcA, 71, 123, doi: [10.32023/0001-5237/71.2.4](https://doi.org/10.32023/0001-5237/71.2.4)

Applegate, J. H. 1992, ApJ, 385, 621, doi: [10.1086/170967](https://doi.org/10.1086/170967)

Arbutina, B. 2007, MNRAS, 377, 1635, doi: [10.1111/j.1365-2966.2007.11723.x](https://doi.org/10.1111/j.1365-2966.2007.11723.x)

Basri, G., & Burgasser, A. J. 2023, Brown Dwarf, ed. M. Gargaud, W. M. Irvine, R. Amils, P. Claeys, H. J. Cleaves, M. Gerin, D. Rouan, T. Spohn, S. Tirard, & M. Viso (Berlin, Heidelberg: Springer Berlin Heidelberg), 435–440, doi: [10.1007/978-3-662-65093-6_208](https://doi.org/10.1007/978-3-662-65093-6_208)

Binnendijk, L. 1960, AJ, 65, 358, doi: [10.1086/108270](https://doi.org/10.1086/108270)

Binnendijk, L. 1970, Vistas in Astronomy, 12, 217, doi: [10.1016/0083-6656\(70\)90041-3](https://doi.org/10.1016/0083-6656(70)90041-3)

Brassieur, C. E., Phillip, C., Fleming, S. W., Mullally, S. E., & White, R. L. 2019, Astrocot: Tools for creating cutouts of TESS images,, Astrophysics Source Code Library, record ascl:1905.007

Table A1. Photometric Solutions and Fitting Results of $O - C$ for V2790 Ori from Previous and This Studies

| Parameters | Photometric Solutions | | | | |
|-------------------------------|--|--|---------------------------------------|---|----------------------------------|
| | E. J. Michaelis (2016) (AAVSO 2015) | W. Kriwattanawong & K. Kriwattanawong (2019) (TNO 2015) | A. Shokry et al. (2020) (KAO 2017) | K. B. Alton & K. Stepien (2021) (DBO 2020) | This study |
| q | 0.317(1) | 0.341(0) | 0.312(0) | 0.304(1) | 0.322(3) |
| $T_1(K)$ | 5471 | 5644 | 5446(12) | 5590 | 5314 |
| $T_2(K)$ | 5620(4) | 5856(9) | 5567 | 5802(2) | 5489(2) |
| $d(^{\circ})$ | 84.15(20) | 85.1(2) | 82.7(2) | 84.93(19) | 84.3(2) |
| $L_{2B}/(L_{1B} + L_{2B})$ | — | 0.3229(10) | — | 0.3025(2) | 0.3105(6) |
| $L_{2V}/(L_{1V} + L_{2V})$ | — | 0.3106(7) | 0.277(25) | 0.2889(1) | 0.2993(4) |
| $L_{2RC}/(L_1R_C + L_2R_C)$ | — | 0.3048(6) | 0.274(14) | — | 0.2934(4) |
| $L_{2lC}/(L_{1lC} + L_{2lC})$ | — | — | 0.284(30) | 0.2784(1) | 0.2892(3) |
| $L_{2g'}/(L_{1g'} + L_{2g'})$ | 0.2966(7) | — | — | — | 0.3054(5) |
| $L_{2r'}/(L_{1r'} + L_{2r'})$ | 0.2867(5) | — | — | — | 0.2943(4) |
| $L_{2l'}/(L_{1l'} + L_{2l'})$ | 0.2830(5) | — | — | — | 0.2899(3) |
| $L_{2T}/(L_{1T} + L_{2T})$ | — | — | — | — | 0.2898(3) |
| r_1 | — | 0.4865(99) | 0.4854 | 0.4878(2) | 0.4861(2) |
| r_2 | — | 0.3011(133) | 0.2693 | 0.2824(2) | 0.2928(4) |
| $f(\%)$ | 15(2) | 20.89(1.03) | 12.8(1.6) | 5.0(5) | 14.8(0.6) |
| Spot 1 | Cool spot | — | Hot spot | — | — |
| Colatitude ($^{\circ}$) | 78(4) | — | 90 | — | — |
| Longitude ($^{\circ}$) | 2(1) | — | 80 | — | — |
| Angular Radius ($^{\circ}$) | 12(4) | — | 11 | — | — |
| T-factor | 0.9(0.5) | — | 1.2 | — | — |
| Spot 2 | Hot spot | Cool spot | — | Cool spot | — |
| Colatitude ($^{\circ}$) | 105(5) | 37(3) | — | 90(4) | — |
| Longitude ($^{\circ}$) | 10(3) | 264(4) | — | 179.5(5) | — |
| Angular Radius ($^{\circ}$) | 14(4) | 26(2) | — | 12.0(1) | — |
| T-factor | 1.16(5) | 0.90(3) | — | 0.75(1) | — |
| Fitting Results of $O - C$ | | | | | |
| ΔT_0 (days) | — | $-5(\pm 21) \times 10^{-5}$ | — | $1.25(\pm 1.80) \times 10^{-4}$ | — |
| ΔP_0 | — | $1.67(\pm 4.45) \times 10^{-7}$ | — | $-6.44(\pm 2.34) \times 10^{-8}$ | — |
| \dot{P} (d yr $^{-1}$) | — | $1.03(\pm 1.43) \times 10^{-7}$ | — | $-2.22(\pm 0.01) \times 10^{-8}$ | $-3.18(\pm 0.75) \times 10^{-8}$ |
| A (days) | — | — | — | $1.7(\pm 0.6) \times 10^{-3}$ | $8.98(\pm 2.19) \times 10^{-4}$ |
| ω ($^{\circ}$) | — | — | — | — | — |
| P_3 (yr) | — | — | — | 6.32(± 0.16) | 7.44(± 0.52) |
| T_3 | — | — | — | — | — |
| ϕ ($^{\circ}$) | — | — | — | — | 256.26(± 11.01) |

Note.—The table summarizes the photometric solutions and orbital period variation analyses of V2790 Ori reported in previous studies, together with the results obtained in this work for comparison. Note that E. J. Michaelis (2016) and A. Shokry et al. (2020) did not perform orbital period variation studies, so their results are not included in the table.

Table A2. Photometric Data of V2790 Ori (Our Observations)

| LCs | Time (BJD) | Δm_B | Time (BJD) | Δm_V | Time (BJD) | Δm_{R_C} | Time (BJD) | Δm_{I_C} |
|----------------------|---------------|--------------|---------------|--------------|---------------|------------------|---------------|------------------|
| 2015 Feb 05 & Mar 06 | 2457058.93893 | 0.326 | 2457058.93932 | 0.490 | 2457058.93971 | 0.569 | 2457058.93997 | 0.604 |
| | 2457058.94038 | 0.316 | 2457058.94077 | 0.479 | 2457058.94116 | 0.552 | 2457058.94142 | 0.598 |
| | 2457058.94183 | 0.309 | 2457058.94221 | 0.466 | 2457058.94261 | 0.547 | 2457058.94287 | 0.587 |
| | 2457058.94328 | 0.297 | 2457058.94367 | 0.461 | 2457058.94405 | 0.538 | 2457058.94431 | 0.579 |
| | 2457058.94472 | 0.293 | 2457058.94511 | 0.453 | 2457058.94550 | 0.528 | 2457058.94576 | 0.571 |
| | 2457058.94617 | 0.278 | 2457058.94656 | 0.448 | 2457058.94695 | 0.524 | 2457058.94721 | 0.563 |
| | 2457058.94762 | 0.277 | 2457058.94801 | 0.438 | 2457058.94898 | 0.509 | 2457058.94980 | 0.551 |
| | 2457058.95021 | 0.261 | 2457058.95060 | 0.426 | 2457058.95132 | 0.500 | 2457058.95158 | 0.545 |
| | 2457058.95199 | 0.257 | 2457058.95238 | 0.419 | 2457058.95276 | 0.496 | 2457058.95302 | 0.539 |
| | 2457058.95343 | 0.248 | 2457058.95382 | 0.415 | 2457058.95420 | 0.490 | 2457058.95446 | 0.532 |
| ... | ... | ... | ... | ... | ... | ... | ... | ... |

NOTE—This table is available in its entirety in machine-readable form in the online journal. A portion is shown here for guidance regarding its form and content.

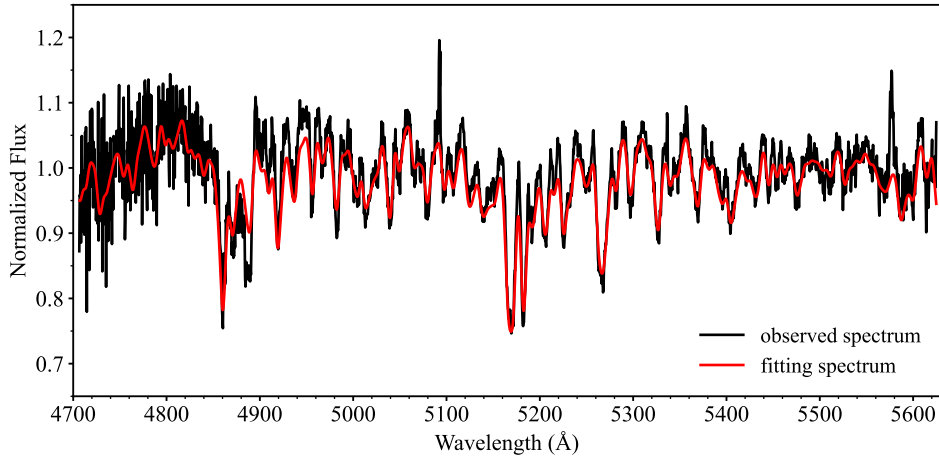


Figure A1. Spectra of BFOSC near phase 0. The black solid line is the observed spectra, while the red solid line is the fitting spectra obtained by ULYSS.

Table A3. Radial Velocities of V2790 Ori

| Time (BJD) | Phase | RV _L | Errors | RV _M | Errors |
|---------------|---------|-----------------|--------|-----------------|--------|
| 2458848.17407 | 0.18026 | — | — | 0.7 | 1.7 |
| 2458848.18456 | 0.21669 | -256.4 | 16.0 | 32.8 | 11.5 |
| 2458848.19505 | 0.25312 | -326.2 | 5.6 | -1.0 | 5.8 |
| 2458848.26667 | 0.50194 | -50.6 | 3.1 | — | — |
| 2458848.30469 | 0.63403 | 141.9 | 8.0 | -105.9 | 6.5 |
| 2458848.31517 | 0.67046 | 177.6 | 20.5 | -133.3 | 13.1 |
| 2458848.32566 | 0.70689 | 181.5 | 11.1 | -94.0 | 9.3 |
| 2458848.33614 | 0.74332 | 204.9 | 14.4 | -120.2 | 9.0 |
| 2459536.13018 | 0.23115 | -313.6 | 2.3 | 9.8 | 1.6 |
| 2459536.14069 | 0.26937 | -305.0 | 2.9 | 10.8 | 2.0 |
| 2459536.15120 | 0.30411 | -292.4 | 3.2 | 15.6 | 2.1 |
| 2459536.16170 | 0.34233 | -266.8 | 4.8 | 9.6 | 3.5 |
| 2459536.17221 | 0.37707 | -224.8 | 8.2 | 20.2 | 6.0 |
| 2459536.18270 | 0.41528 | -202.6 | 10.6 | 5.6 | 7.8 |
| 2459536.19321 | 0.45002 | — | — | -27.5 | 1.2 |
| 2459536.29315 | 0.79744 | 199.2 | 4.2 | -105.3 | 2.7 |
| 2459536.30366 | 0.83565 | 187.4 | 4.9 | -103.4 | 3.1 |
| 2459536.31422 | 0.87039 | 144.1 | 6.7 | -109.1 | 10.7 |
| 2459536.32473 | 0.90861 | 132.5 | 5.9 | -84.8 | 4.4 |
| 2459536.33524 | 0.94335 | — | — | -54.4 | 1.2 |

NOTE—RV_L represents the radial velocities of the less massive components, while RV_M represents the radial velocities of the more massive components.

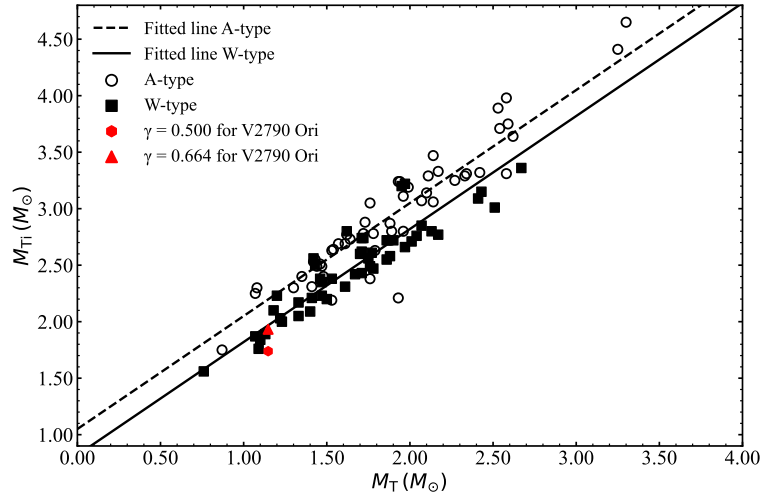


Figure A2. The relation between present total mass M_T and initial total mass M_{Ti} for A-subtype and W-subtype contact binaries from M. Yıldız (2014) using a sample of 51 A-subtype (open circles) and 49 W-subtype (solid circles) contact systems, respectively. The position of V2790 Ori ($\gamma = 0.597$) is marked with a red solid star.

Table A4. Spot Parameters of V2790 Ori

| LCs | Spot 1 | | | Spot 2 | | |
|------------------------------|---------------|--------------------|----------|---------------|--------------------|----------|
| | Longitude (°) | Angular Radius (°) | T-factor | Longitude (°) | Angular Radius (°) | T-factor |
| 2015 Feb 05 & Mar 06 | 183.4 | 18.1 | 0.726 | 158.8 | 8.2 | 0.718 |
| 2015 Dec 28 | 354.1 | 11.8 | 0.726 | 165.0 | 9.1 | 0.718 |
| 2016 Dec 30 | 130.3 | 24.3 | 0.728 | 186.9 | 10.0 | 0.704 |
| 2017 Dec 20 | 178.8 | 22.0 | 0.717 | 167.2 | 10.0 | 0.658 |
| 2018 Dec 27 | 320.4 | 5.2 | 0.728 | 263.7 | 5.6 | 0.728 |
| 2019 Dec 29 & 2020 Jan 03 | 328.5 | 18.6 | 0.726 | 258.0 | 13.0 | 0.726 |
| 2020 Dec 20 | 123.2 | 9.6 | 0.898 | 263.4 | 11.7 | 0.580 |
| 2021 Jan 04 & Jan 05 | 332.7 | 5.7 | 0.726 | 98.7 | 6.0 | 0.726 |
| 2022 Jan 02 | 283.9 | 11.1 | 0.726 | 281.5 | 10.4 | 0.726 |
| 2022 Dec 31 | 330.0 | 9.9 | 0.690 | 354.4 | 7.5 | 0.631 |
| 2024 Feb 27 & Mar 08 | 173.8 | 9.0 | 0.724 | 278.7 | 8.7 | 0.724 |
| 2025 Jan 08 | 146.5 | 12.0 | 0.695 | 170.8 | 7.2 | 0.684 |
| AAVSO – 2015 Jan 08 – Jan 29 | 173.1 | 18.1 | 0.768 | 164.9 | 8.1 | 0.768 |
| AAVSO – 2015 Nov 19 & Nov 20 | 177.1 | 20.0 | 0.707 | 167.5 | 8.7 | 0.635 |
| AAVSO – 2020 Jan 29 – Feb 05 | 198.9 | 11.0 | 0.645 | 180.7 | 13.3 | 0.686 |
| TESS – S43 | 30.0 | 14.0 | 0.726 | 334.0 | 14.1 | 0.726 |
| TESS – S44 | 32.4 | 8.4 | 0.704 | 314.9 | 13.8 | 0.740 |
| TESS – S45 | 31.0 | 11.7 | 0.728 | 327.7 | 12.8 | 0.728 |
| TESS – S71 | 340.8 | 18.0 | 0.726 | 282.8 | 13.4 | 0.726 |
| TESS – S72 | 346.4 | 19.3 | 0.738 | 277.6 | 14.3 | 0.732 |
| TNO – 2015 Jan 21 – Jan 23 | 190.9 | 19.6 | 0.756 | 176.5 | 12.0 | 0.742 |
| KAO – 2017 Jan 21 & Jan 22 | 119.2 | 20.5 | 0.742 | 339.7 | 9.0 | 0.695 |

NOTE—Spot 1 is on the primary component, and Spot 2 is on the secondary component.

Table A5. Eclipsing Minima of V2790 Ori

| BJD | Error | Epoch | $(O - C)_1$ | $(O - C)_2$ | Res. | Ref. |
|--------------|--------|----------|-------------|-------------|---------|------|
| 2451521.6950 | 0.0005 | -24175 | -0.0044 | 0.0012 | 0.0005 | 1 |
| 2453327.7560 | 0.0004 | -17900.5 | -0.0034 | -0.0007 | 0.0002 | 2 |
| 2455520.8205 | 0.0002 | -10281.5 | -0.0015 | -0.0009 | -0.0003 | 3 |
| 2455532.9103 | 0.0004 | -10239.5 | -0.0010 | -0.0005 | 0.0002 | 2 |
| 2455604.2950 | 0.0004 | -9991.5 | -0.0009 | -0.0004 | 0.0003 | 3 |
| 2455632.3597 | 0.0004 | -9894 | -0.0007 | -0.0003 | 0.0005 | 3 |
| 2455644.3050 | 0.0004 | -9852.5 | -0.0009 | -0.0004 | 0.0004 | 3 |
| 2455896.8827 | 0.0003 | -8975 | -0.0039 | -0.0036 | -0.0027 | 4 |
| 2455902.7850 | 0.0001 | -8954.5 | -0.0023 | -0.0020 | -0.0011 | 5 |
| 2455959.3466 | 0.0002 | -8758 | -0.0015 | -0.0013 | -0.0004 | 6 |
| 2456288.0610 | 0.0004 | -7616 | -0.0018 | -0.0017 | -0.0012 | 7 |
| 2456288.2045 | 0.0004 | -7615.5 | -0.0023 | -0.0022 | -0.0017 | 7 |
| 2456623.1092 | 0.0004 | -6452 | -0.0009 | -0.0009 | -0.0011 | 8 |
| 2456623.2547 | 0.0004 | -6451.5 | 0.0007 | 0.0007 | 0.0005 | 8 |
| 2457030.6939 | 0.0004 | -5036 | 0.0007 | 0.0005 | -0.0003 | 9 |
| ... | ... | ... | ... | ... | ... | ... |

NOTE—Ref. 1. S. A. Otero et al. (2004); 2. R. Diethelm (2011); 3. K. Nagai (2012); 4. R. Diethelm (2012); 5. R. H. Nelson (2012); 6. J. Hubscher (2013); 7. K. Nagai (2013); 8. K. Hirosawa (2013); 9. AAVSO; 10. W. Kriwattanawong & K. Kriwattanawong (2019); 11. Our data; 12. J. Juryšek et al. (2017); 13. R. Nelson (2016); 14. ASAS-SN; 15. K. Nagai (2016); 16. A. Shokry et al. (2020); 17. BRNO; 18. TESS; 19. K. Nagai (2023); This table is available in its entirety in machine-readable form in the online journal. A portion is shown here for guidance regarding its form and content.

Chambliss, C. R. 1992, in IAU Symposium, Vol. 151, Evolutionary Processes in Interacting Binary Stars, ed. Y. Kondo, R. Sistero, & R. S. Polidan, 315

Christopoulou, P. E., & Papageorgiou, A. 2013, AJ, 146, 157, doi: [10.1088/0004-6256/146/6/157](https://doi.org/10.1088/0004-6256/146/6/157)

Diethelm, R. 2011, Information Bulletin on Variable Stars, 5960, 1

Diethelm, R. 2012, Information Bulletin on Variable Stars, 1. <https://ibvs.konkoly.hu/pub/ibvs/6011.pdf>

Eastman, J., Siverd, R., & Gaudi, B. S. 2010, PASP, 122, 935, doi: [10.1086/655938](https://doi.org/10.1086/655938)

Eggleton, P. P. 2012, Journal of Astronomy and Space Sciences, 29, 145, doi: [10.5140/JASS.2012.29.2.145](https://doi.org/10.5140/JASS.2012.29.2.145)

Eggleton, P. P., & Kisselava-Eggleton, L. 2006, Ap&SS, 304, 75, doi: [10.1007/s10509-006-9078-z](https://doi.org/10.1007/s10509-006-9078-z)

Eker, Z., Demircan, O., & Bilir, S. 2008, Monthly Notices of the Royal Astronomical Society, 386, 1756, doi: [10.1111/j.1365-2966.2008.13155.x](https://doi.org/10.1111/j.1365-2966.2008.13155.x)

Eker, Z., Demircan, O., Bilir, S., & Karataş, Y. 2006, MNRAS, 373, 1483, doi: [10.1111/j.1365-2966.2006.11073.x](https://doi.org/10.1111/j.1365-2966.2006.11073.x)

Fabrycky, D., & Tremaine, S. 2007, ApJ, 669, 1298, doi: [10.1086/521702](https://doi.org/10.1086/521702)

Fan, Z., Wang, H., Jiang, X., et al. 2016, PASP, 128, 115005, doi: [10.1088/1538-3873/128/969/115005](https://doi.org/10.1088/1538-3873/128/969/115005)

Gettel, S. J., Geske, M. T., & McKay, T. A. 2006, AJ, 131, 621, doi: [10.1086/498016](https://doi.org/10.1086/498016)

Guinan, E. F., & Bradstreet, D. H. 1988, in NATO Advanced Study Institute (ASI) Series C, Vol. 241, Formation and Evolution of Low Mass Stars, ed. A. K. Dupree & M. T. V. T. Lago, 345, doi: [10.1007/978-94-009-3037-7_23](https://doi.org/10.1007/978-94-009-3037-7_23)

Gull, M., Weisz, D. R., El-Badry, K., et al. 2025, ApJ, 986, 25, doi: [10.3847/1538-4357/adca39](https://doi.org/10.3847/1538-4357/adca39)

Hilditch, R. W. 2001, An Introduction to Close Binary Stars

Hirosawa, K. 2013, Variable Star Bulletin, 54, 1

Hu, K., Yu, Y.-X., Zhang, J.-F., & Xiang, F.-Y. 2020, AJ, 160, 62, doi: [10.3847/1538-3881/ab99c4](https://doi.org/10.3847/1538-3881/ab99c4)

Hu, S. M., Han, S.-H., Guo, D.-F., & Du, J.-J. 2014, Research in Astronomy and Astrophysics, 14, 719, doi: [10.1088/1674-4527/14/6/010](https://doi.org/10.1088/1674-4527/14/6/010)

Hubscher, J. 2013, Information Bulletin on Variable Stars, 6084, 1

Hurley, J. R., Tout, C. A., & Pols, O. R. 2002, MNRAS, 329, 897, doi: [10.1046/j.1365-8711.2002.05038.x](https://doi.org/10.1046/j.1365-8711.2002.05038.x)

Table A6. Measurements of the O'Connell Effect in the Light Curves of V2790 Ori

| LCs | Mean Epoch | Band | Δm (mag) | OER | Min.I - Min.II | Max.I - Min.II | Max.II - Min.II |
|----------------------|------------|----------------------|------------------|--------|----------------|----------------|-----------------|
| 2015 Feb 05 & Mar 06 | -4837 | <i>B</i> | -0.0051 | 0.9796 | 0.0132 | -0.6074 | -0.6125 |
| | | <i>V</i> | -0.0054 | 0.9801 | 0.0053 | -0.5651 | -0.5706 |
| | | <i>R_C</i> | -0.0055 | 0.9812 | 0.0035 | -0.5399 | -0.5454 |
| | | <i>I_C</i> | -0.0054 | 0.9826 | 0.0058 | -0.5169 | -0.5222 |
| 2015 Dec 28 | -3804 | <i>B</i> | -0.0062 | 0.9806 | 0.0474 | -0.5704 | -0.5765 |
| | | <i>V</i> | -0.0066 | 0.9805 | 0.0391 | -0.5342 | -0.5407 |
| | | <i>R_C</i> | -0.0067 | 0.9812 | 0.0348 | -0.5136 | -0.5203 |
| | | <i>I_C</i> | -0.0066 | 0.9823 | 0.0340 | -0.4949 | -0.5016 |
| 2016 Dec 30 | -2626 | <i>B</i> | 0.0460 | 1.1035 | -0.0020 | -0.6073 | -0.5613 |
| | | <i>V</i> | 0.0421 | 1.0986 | -0.0028 | -0.5687 | -0.5266 |
| | | <i>R_C</i> | 0.0386 | 1.0924 | -0.0024 | -0.5453 | -0.5067 |
| | | <i>I_C</i> | 0.0350 | 1.0852 | 0.0009 | -0.5236 | -0.4886 |
| 2017 Dec 20 | -1293 | <i>B</i> | -0.0018 | 0.9868 | -0.0003 | -0.5902 | -0.5971 |
| | | <i>V</i> | -0.0022 | 0.9867 | -0.0044 | -0.5521 | -0.5558 |
| | | <i>R_C</i> | -0.0024 | 0.9871 | -0.0045 | -0.5299 | -0.5308 |
| | | <i>I_C</i> | -0.0026 | 0.9878 | -0.0011 | -0.5099 | -0.5077 |
| 2018 Dec 27 | 0 | <i>B</i> | 0.0063 | 1.0087 | 0.0776 | -0.5692 | -0.5630 |
| | | <i>V</i> | 0.0058 | 1.0093 | 0.0552 | -0.5369 | -0.5311 |
| | | <i>R_C</i> | 0.0052 | 1.0092 | 0.0456 | -0.5184 | -0.5132 |
| | | <i>I_C</i> | 0.0046 | 1.0089 | 0.0420 | -0.5011 | -0.4965 |
| ... | ... | ... | ... | ... | ... | ... | ... |

NOTE—This table is available in its entirety in machine-readable form in the online journal. A portion is shown here for guidance regarding its form and content.

Iglesias-Marzoa, R., López-Morales, M., & Jesús Arévalo Morales, M. 2015, rvfit: Radial velocity curves fitting for binary stars or exoplanets., Astrophysics Source Code Library, record ascl:1505.020

Irwin, J. B. 1952, ApJ, 116, 211, doi: [10.1086/145604](https://doi.org/10.1086/145604)

Irwin, J. B. 1959, AJ, 64, 149, doi: [10.1086/107913](https://doi.org/10.1086/107913)

Jayasinghe, T., Stanek, K. Z., Kochanek, C. S., et al. 2019, MNRAS, 486, 1907, doi: [10.1093/mnras/stz844](https://doi.org/10.1093/mnras/stz844)

Jenkins, J. M., Twicken, J. D., McCauliff, S., et al. 2016, in Society of Photo-Optical Instrumentation Engineers (SPIE) Conference Series, Vol. 9913, Software and Cyberinfrastructure for Astronomy IV, ed. G. Chiozzi & J. C. Guzman, 99133E, doi: [10.1117/12.2233418](https://doi.org/10.1117/12.2233418)

Juryšek, J., Hořkovičová, K., Šmelcer, L., et al. 2017, Open European Journal on Variable Stars, 179, 1

Knote, M. F. 2021, in American Astronomical Society Meeting Abstracts, Vol. 237, American Astronomical Society Meeting Abstracts, 418.07D

Knote, M. F., Caballero-Nieves, S. M., Gokhale, V., Johnston, K. B., & Perlman, E. S. 2022, ApJS, 262, 10, doi: [10.3847/1538-4365/ac770f](https://doi.org/10.3847/1538-4365/ac770f)

Koleva, M., Prugniel, P., Bouchard, A., & Wu, Y. 2009, A&A, 501, 1269, doi: [10.1051/0004-6361/200811467](https://doi.org/10.1051/0004-6361/200811467)

Kopal, Z. 1959, Close binary systems

Kozai, Y. 1962, AJ, 67, 591, doi: [10.1086/108790](https://doi.org/10.1086/108790)

Kriwattanawong, W., & Kriwattanawong, K. 2019, Research in Astronomy and Astrophysics, 19, 143, doi: [10.1088/1674-4527/19/10/143](https://doi.org/10.1088/1674-4527/19/10/143)

Kuiper, G. P. 1941, ApJ, 93, 133, doi: [10.1086/144252](https://doi.org/10.1086/144252)

Kwee, K. K., & van Woerden, H. 1956, BAN, 12, 327

Landin, N. R., Mendes, L. T. S., & Vaz, L. P. R. 2009, A&A, 494, 209, doi: [10.1051/0004-6361:20078403](https://doi.org/10.1051/0004-6361:20078403)

Lanza, A. F., & Rodonò, M. 1999, A&A, 349, 887

Lanza, A. F., & Rodonò, M. 2002, Astronomische Nachrichten, 323, 424, doi: [10.1002/1521-3994\(200208\)323:3/4<424::AID-ASNA424>3.0.CO;2-1](https://doi.org/10.1002/1521-3994(200208)323:3/4<424::AID-ASNA424>3.0.CO;2-1)

Li, K., Gao, D. Y., Hu, S. M., et al. 2016, Ap&SS, 361, 63, doi: [10.1007/s10509-016-2649-8](https://doi.org/10.1007/s10509-016-2649-8)

Li, K., Gao, X., Liu, X.-Y., et al. 2022, AJ, 164, 202, doi: [10.3847/1538-3881/ac8ff2](https://doi.org/10.3847/1538-3881/ac8ff2)

Li, K., Kim, C.-H., Xia, Q.-Q., et al. 2020, AJ, 159, 189, doi: [10.3847/1538-3881/ab7cda](https://doi.org/10.3847/1538-3881/ab7cda)

Li, K., & Qian, S. B. 2013, *NewA*, 21, 46, doi: [10.1016/j.newast.2012.11.003](https://doi.org/10.1016/j.newast.2012.11.003)

Li, K., Qian, S. B., Hu, S. M., & He, J. J. 2014, *AJ*, 147, 98, doi: [10.1088/0004-6256/147/5/98](https://doi.org/10.1088/0004-6256/147/5/98)

Li, K., Xia, Q. Q., Hu, S. M., Guo, D. F., & Chen, X. 2018, *PASP*, 130, 074201, doi: [10.1088/1538-3873/aac067](https://doi.org/10.1088/1538-3873/aac067)

Li, K., Xia, Q.-Q., Kim, C.-H., et al. 2021a, *ApJ*, 922, 122, doi: [10.3847/1538-4357/ac242f](https://doi.org/10.3847/1538-4357/ac242f)

Li, K., Xia, Q.-Q., Liu, J.-Z., et al. 2019, *Research in Astronomy and Astrophysics*, 19, 147, doi: [10.1088/1674-4527/19/10/147](https://doi.org/10.1088/1674-4527/19/10/147)

Li, K., Xia, Q.-Q., Kim, C.-H., et al. 2021b, *AJ*, 162, 13, doi: [10.3847/1538-3881/abfc53](https://doi.org/10.3847/1538-3881/abfc53)

Li, L., Zhang, F., Han, Z., & Jiang, D. 2007, *ApJ*, 662, 596, doi: [10.1086/517909](https://doi.org/10.1086/517909)

Liao, W. P., & Qian, S. B. 2010, *MNRAS*, 405, 1930, doi: [10.1111/j.1365-2966.2010.16584.x](https://doi.org/10.1111/j.1365-2966.2010.16584.x)

Lightkurve Collaboration, Cardoso, J. V. d. M., Hedges, C., et al. 2018, Lightkurve: Kepler and TESS time series analysis in Python., *Astrophysics Source Code Library*, record ascl:1812.013

Liu, L. 2021, *PASP*, 133, 084202, doi: [10.1088/1538-3873/ac1ac1](https://doi.org/10.1088/1538-3873/ac1ac1)

Liu, N.-P., Sarotsakulchai, T., Rattanasoon, S., & Zhang, B. 2020, *PASJ*, 72, 73, doi: [10.1093/pasj/pssaa062](https://doi.org/10.1093/pasj/pssaa062)

Liu, Q.-Y., & Yang, Y.-L. 2003, *ChJA&A*, 3, 142, doi: [10.1088/1009-9271/3/2/142](https://doi.org/10.1088/1009-9271/3/2/142)

Liu, X.-Y., Li, K., Michel, R., et al. 2023, *MNRAS*, 519, 5760, doi: [10.1093/mnras/stad026](https://doi.org/10.1093/mnras/stad026)

Lucy, L. B. 1967, *ZA*, 65, 89

Lucy, L. B. 1968a, *ApJ*, 151, 1123, doi: [10.1086/149510](https://doi.org/10.1086/149510)

Lucy, L. B. 1968b, *ApJ*, 153, 877, doi: [10.1086/149712](https://doi.org/10.1086/149712)

Maceroni, C., & Rucinski, S. M. 1997, *PASP*, 109, 782, doi: [10.1086/133944](https://doi.org/10.1086/133944)

Matijević, G., Zwitter, T., Munari, U., et al. 2010, *AJ*, 140, 184, doi: [10.1088/0004-6256/140/1/184](https://doi.org/10.1088/0004-6256/140/1/184)

Mayer, P. 1990, *Bulletin of the Astronomical Institutes of Czechoslovakia*, 41, 231

McCartney, S. 1997, in *Astronomical Society of the Pacific Conference Series*, Vol. 130, The Third Pacific Rim Conference on Recent Development on Binary Star Research, ed. K.-C. Leung, 129

Meng, Z.-B., Wu, P.-R., Yu, Y.-X., Hu, K., & Xiang, F.-Y. 2024, *ApJ*, 971, 113, doi: [10.3847/1538-4357/ad571e](https://doi.org/10.3847/1538-4357/ad571e)

Michaels, E. J. 2016, *JAAVSO*, 44, 30

Nagai, K. 2012, *Variable Star Bulletin*, 53, 1

Nagai, K. 2013, *Variable Star Bulletin*, 55, 1

Nagai, K. 2016, *Variable Star Bulletin*, 1

Nagai, K. 2023, *Variable Star Bulletin*, 1

Nelson, R. 2016, *Information Bulletin on Variable Stars*

Nelson, R. H. 2012, *Information Bulletin on Variable Stars*, 6018, 1

O'Connell, D. J. K. 1951, *Publications of the Riverview College Observatory*, 2, 85

Oelkers, R. J., & Stassun, K. G. 2018, *AJ*, 156, 132, doi: [10.3847/1538-3881/aad68e](https://doi.org/10.3847/1538-3881/aad68e)

Oliphant, T. E. 2007, *Computing in Science and Engineering*, 9, 10, doi: [10.1109/MCSE.2007.58](https://doi.org/10.1109/MCSE.2007.58)

Otero, S. A., Wils, P., & Dubovsky, P. A. 2004, *Information Bulletin on Variable Stars*, 5570, 1

Paczynski, B. 1971, *ARA&A*, 9, 183

Pecaut, M. J., & Mamajek, E. E. 2013, *ApJS*, 208, 9, doi: [10.1088/0067-0049/208/1/9](https://doi.org/10.1088/0067-0049/208/1/9)

Poro, A., Li, K., Michel, R., et al. 2024, *AJ*, 168, 272, doi: [10.3847/1538-3881/ad8345](https://doi.org/10.3847/1538-3881/ad8345)

Poro, A., Li, K., Paki, E., et al. 2025, *MNRAS*, 537, 3160, doi: [10.1093/mnras/staf222](https://doi.org/10.1093/mnras/staf222)

Pringle, J. E. 1975, *MNRAS*, 170, 633, doi: [10.1093/mnras/170.3.633](https://doi.org/10.1093/mnras/170.3.633)

Prugniel, P., & Soubiran, C. 2001, *A&A*, 369, 1048, doi: [10.1051/0004-6361:20010163](https://doi.org/10.1051/0004-6361:20010163)

Qian, S. 2003, *MNRAS*, 342, 1260, doi: [10.1046/j.1365-8711.2003.06627.x](https://doi.org/10.1046/j.1365-8711.2003.06627.x)

Qian, S.-B., Yang, Y.-G., Soonthornthum, B., et al. 2005, *AJ*, 130, 224, doi: [10.1086/430673](https://doi.org/10.1086/430673)

Qian, S. B., Wang, J. J., Zhu, L. Y., et al. 2014, *ApJS*, 212, 4, doi: [10.1088/0067-0049/212/1/4](https://doi.org/10.1088/0067-0049/212/1/4)

Rahunen, T. 1981, *A&A*, 102, 81

Ricker, G. R., Winn, J. N., Vanderspek, R., et al. 2015, *Journal of Astronomical Telescopes, Instruments, and Systems*, 1, 014003, doi: [10.1117/1.JATIS.1.1.014003](https://doi.org/10.1117/1.JATIS.1.1.014003)

Riener, M., Kainulainen, J., Henshaw, J. D., et al. 2019, *A&A*, 628, A78, doi: [10.1051/0004-6361/201935519](https://doi.org/10.1051/0004-6361/201935519)

Ruciński, S. M. 1969, *AcA*, 19, 245

Ruciński, S. M., Pribulla, T., & van Kerkwijk, M. H. 2007, *AJ*, 134, 2353, doi: [10.1086/523353](https://doi.org/10.1086/523353)

Shappee, B. J., Prieto, J. L., Grupe, D., et al. 2014, *ApJ*, 788, 48, doi: [10.1088/0004-637X/788/1/48](https://doi.org/10.1088/0004-637X/788/1/48)

Shaw, J. S. 1994, *Mem. Soc. Astron. Italiana*, 65, 95

Shokry, A., Zead, I. Z., El-Depsey, M. H., et al. 2020, *NewA*, 80, 101400, doi: [10.1016/j.newast.2020.101400](https://doi.org/10.1016/j.newast.2020.101400)

Smith, R. C. 1984, *QJRAS*, 25, 405

Southworth, J., Bruntt, H., & Buzasi, D. L. 2007, *A&A*, 467, 1215, doi: [10.1051/0004-6361:20077184](https://doi.org/10.1051/0004-6361:20077184)

Szalai, T., Kiss, L. L., Mészáros, S., Vinkó, J., & Csizmadia, S. 2007, *A&A*, 465, 943, doi: [10.1051/0004-6361:20066768](https://doi.org/10.1051/0004-6361:20066768)

Tout, C. A., & Eggleton, P. P. 1988, *MNRAS*, 231, 823

Van Hamme. 1993, *AJ*, 106, 2096, doi: [10.1086/116788](https://doi.org/10.1086/116788)

vant Veer, F. 1979, *A&A*, 80, 287

Wang, J.-J., Guo, M., Tian, X.-M., & Zhang, B. 2025, *Research in Astronomy and Astrophysics*, 25, 025006, doi: [10.1088/1674-4527/ada424](https://doi.org/10.1088/1674-4527/ada424)

Weber, E. J., & Davis, Jr., L. 1967, ApJ, 148, 217, doi: [10.1086/149138](https://doi.org/10.1086/149138)

Wilsey, N. J., & Beaky, M. M. 2009, Society for Astronomical Sciences Annual Symposium, 28, 107

Wilson, R. E. 1979, ApJ, 234, 1054, doi: [10.1086/157588](https://doi.org/10.1086/157588)

Wilson, R. E. 1990, ApJ, 356, 613, doi: [10.1086/168867](https://doi.org/10.1086/168867)

Wilson, R. E., & Devinney, E. J. 1971, ApJ, 166, 605, doi: [10.1086/150986](https://doi.org/10.1086/150986)

Woltjer, Jr., J. 1922, BAN, 1, 93

Wozniak, P. R., Vestrand, W. T., Akerlof, C. W., et al. 2004, VizieR Online Data Catalog: Northern Sky Variability Survey (NSVS) (Wozniak+, 2004),, VizieR On-line Data Catalog: II/287. Originally published in: 2004AJ....127.2436W

Yakut, K., & Eggleton, P. P. 2005, ApJ, 629, 1055, doi: [10.1086/431300](https://doi.org/10.1086/431300)

Yıldız, M. 2014, MNRAS, 437, 185, doi: [10.1093/mnras/stt1874](https://doi.org/10.1093/mnras/stt1874)

Yıldız, M., & Doğan, T. 2013, MNRAS, 430, 2029, doi: [10.1093/mnras/stt028](https://doi.org/10.1093/mnras/stt028)

Yılmaz, M., Şenavcı, H. V., Bahar, E., et al. 2023, NewA, 101, 102022, doi: [10.1016/j.newast.2023.102022](https://doi.org/10.1016/j.newast.2023.102022)

Zhang, B., Gao, Y.-D., Li, K., et al. 2025, Monthly Notices of the Royal Astronomical Society, 537, 3366, doi: [10.1093/mnras/staf216](https://doi.org/10.1093/mnras/staf216)

Zhang, X., & Zhang, B. 2024, Research in Astronomy and Astrophysics, 24, 015022, doi: [10.1088/1674-4527/ad1367](https://doi.org/10.1088/1674-4527/ad1367)

Zhou, D.-Q., & Leung, K.-C. 1990, ApJ, 355, 271, doi: [10.1086/168760](https://doi.org/10.1086/168760)

Zhou, X. 2025, Monthly Notices of the Royal Astronomical Society, 541, 3401, doi: [10.1093/mnras/staf1170](https://doi.org/10.1093/mnras/staf1170)